Important Notice

UNIVERSITY OF CALGARY

Time-lapse Electrical Resistivity Imaging of Methane Gas Migration in a Shallow Confined Aquifer

by

Timothy Alan Cary

A THESIS

SUBMITTED TO THE FACULTY OF GRADUATE STUDIES

IN PARTIAL FULFILMENT OF THE REQUIREMENTS FOR THE

DEGREE OF MASTER OF SCIENCE

GRADUATE PROGRAM IN GEOLOGY AND GEOPHYSICS

CALGARY, ALBERTA

APRIL, 2019

Abstract

In order to quantify, and develop tools to monitor, fugitive methane emissions from well-bore environments, a field experiment was carried out in which an 85% methane composite gas was injected into a near surface confined aquifer at a rate of 1.5 m^3 per day, for 66 days. The site is located in north-eastern British Columbia where the Quaternary glacial deposits are typical of the environment for the majority of energy wells in Western Canada. Temperature corrected time-lapse electrical resistivity tomography (ERT) was utilized to monitor the migration and fate of the gas plume during the injection period. Three permanently installed ERT lines were deployed, centered on or close to the injection location. The data were inverted using SimPEG producing time-lapse difference images. Results show resistivity increases of up to 15% near the injection zone. The gas plume is interpreted as migrating upward and spreading laterally beneath a low permeability layer.

Acknowledgements

Firstly, I would like to thank my supervisors, Dr Lauer and Dr Innanen, for providing me with the opportunity to study for my Master's degree. They provided me with invaluable guidance during my time at the University of Calgary and their unbridled enthusiasm for research helped me push through in times of doubt. I would like to thank Dr. Lauer for allowing me to present my research at AGU 100 and for going above and beyond the requirements of her duty as supervisor.

I would like to thank the industrial sponsors of CREWES, NSERC, and the sponsors of the Geofluids and Geohazards group for funding my research.

I would also like to thank my fellow graduate students Matt Eaid, Bobby Gunning, Tyler Spackman, Scott Keating, and Andrew Mills. The friendships made at CREWES provided a great source of entertainment.

I would like to thank my family for their love and support. Most importantly, my partner in life Sarah Gallagher. Your love and patience in the final months of writing enabled me to fully devote my time to my work. You always encouraged me to keep going and believed in what I was trying to achieve.

Table of Contents

List of Tables

List of Figures and Illustrations

List of Symbols, Abbreviations and Nomenclature

Symbol	Definition
a	Electrode separation
α_s	Model smallness
α_x	Horizontal smoothing parameter
α_z	Vertical smoothing parameter
β	Tikhonov regularization parameter
$\boldsymbol{d}_{obs}$	Observed data
$\boldsymbol{d}_{obs}^{TC}$	Temperature corrected observed data
$\boldsymbol{d}_{est}$	Estimated data
$\boldsymbol{d}_{est}^{TC}$	Temperature corrected estimated data
ε_i	Data error estimate
I	Current
$\boldsymbol{I}$	Identity matrix
$\boldsymbol{J}$	Jacobian matrix
k	Permeability
$\boldsymbol{m}$	Resistivity model
$\boldsymbol{m}_{ref}$	Reference model
ϕ	Porosity
ϕ_d	Data misfit function
ϕ_m	Model misfit function
P_c	Capillary pressure
P_{nw}	Pressure of non-wetting fluid
P_w	Pressure of wetting fluid
ρ	Resistivity
ρ_a	Apparent resistivity
σ	Conductivity
V	Potential
$\boldsymbol{W_d}$	Data weighting matrix
$\boldsymbol{W}_x^T$	Discretized gradient operator in x direction
$\boldsymbol{W}_z^T$	Discretized gradient operator in z direction
z_e	Pseudodepth
API	American Petroleum Institute (Unit)
bgs	Below ground surface
ERT	Electrical resistivity tomography
DNAPL	Dense nonaqueous phase liquid
DTS	Distributed temperature sensing

CHAPTER 1: INTRODUCTION

1.1 Introduction

The unintended release of natural gases from well-bores, primarily comprised of methane (Cahill et al., 2019), is well documented. Previous studies of wells in the UK (Boothroyd et al., 2016) found that of 102 decommissioned onshore wells, 30% had significant increases in soil methane levels. In similar studies of Alberta wells comprising 316,439 wells drilled from 1910-2004, 4.6% were reported to have well integrity failures (Davies et al. 2014), establishing significant potential for fugitive gas migration. Methane poses risks to human health and safety as a greenhouse gas, as a contaminant in groundwater (Van Stempvoort et al., 2005), and if allowed to accumulate, can create a potential explosion hazard (Eltschlager et al., 2001). The recent shift in industry to the use of hydraulic fracturing as a means to enhance extraction has led to a marked increase in the number of wells being drilled for unconventional resources (BC Oil and Gas Commission, 2016). In British Columbia, unconventional gas production increased from 20% to 60% of B.C.'s total gas production from 2005 to 2012 (Rivard et al, 2014). Ingraffea et al. (2014), reported in a Pennsylvania study that unconventional wells are between 1.57-6 times more likely to suffer from integrity failures than conventional wells, depending on the age of the well and the local geology. Therefore, as the unconventional sector continues to grow, there are likely to be more incidents of fugitive methane release.

The migration and evolution of fugitive methane is poorly understood, which is the key motivation for this study. Developing a reliable and efficient monitoring strategy has the

potential to reduce the risks posed by fugitive methane, although the literature on subsurface monitoring of methane gas migration is limited to studies conducted in regions with homogeneous subsurface conditions. For example, Steelman et al (2017) utilized time-lapse ground penetrating radar (GPR) and electrical resistivity tomography (ERT) to monitor the migration of a methane gas plume in an unconfined sandy aquifer at the Borden test site in Ontario, Canada. The field experiment replicated a well-bore leak by injecting methane gas into the saturated shallow subsurface, and monitored the plume using a combination of near surface geophysical methods and borehole data. It was observed that after the initial vertical migration, driven by buoyancy forces, the gas plume spread laterally when encountering heterogeneities in grain size at shallower depths. Specifically, subtle variations in permeability caused by the changes in grain size directed the movement of the gas plume. Steelman et al. (2017) also found that the gas was capable of migrating much greater lateral distances than expected by groundwater advection alone. Numerical modelling of a controlled methane release (Klazinga ,2018) highlighted that migration is primarily driven by buoyancy forces, with groundwater flow as a secondary mechanism. The results showed that, once the gas reached a less permeable layer it spread laterally until the pressure in the plume was great enough to break through the overlying confining layer. Klazinga also utilized ERT simulations to image the main plume near the injector, however, the imaging of thin lateral migration pathways was not possible.

Geophysical methods provide a non-destructive and non-invasive method of observing changes in the subsurface. Additionally, they provide a broad view of the subsurface, whereas conventional monitoring techniques sample discrete points or profiles of the subsurface via monitoring wells. Therefore, the spatial extent of the subsurface changes can be mapped more readily using geophysical methods. Central to this study, electrical resistivity methods are

sensitive to the bulk electrical properties of the soil volume. Accordingly, the displacement of groundwater by immiscible fluids with significantly different electrical properties (e.g. gas) is a problem well suited to monitoring using electrical resistivity methods.

This study aims to expand this area of research, by focusing on a study site characterized by a heterogeneous geological environment that is similar to many of Canada's unconventional oil and gas plays in development. The experimental site is located near Fort St. John, B.C., within a fluvioglacial deposit located on the bluffs on the Peace River. This area is part of the Montney resource play and is home to over 25 000 energy wells (Cahill et al., 2019). The experiment utilizes 18 time-lapse ERT data sets across three ERT profiles to delineate resistivity changes due to gas migration within the aquifer. Distributed temperature sensing (DTS) data provide subsurface temperature profiles that are used to correct the ERT data for temperature effects, thus increasing the confidence in the resistivity changes observed. The time-series data are inverted using a cascaded time-lapse inversion technique (Miller et al, 2008) and the resulting data differences are studied to evaluate the evolution of the position of injected gas in the aquifer.

The thesis is divided into six chapters. Chapter 1 introduces the problem of fugitive methane gas and outlines the motivation for the work that has been done. In Chapter 2 the relevant background theory of multiphase flow, electrical resistivity methods, and distributed temperature sensing are outlined, culminating in a literature review of previous applications of electrical resistivity monitoring of multiphase flow. Chapter 3 contains a description of the experimental field site and monitoring methodology, and Chapter 4 outlines the theory and practice of electrical resistivity inversion used in this study, including the implementation of SimPEG, an open source geophysical inversion framework. Chapters 5 and 6 present the results

and interpretation of the temperature corrected time-lapse inversions, as well as suggested areas of future work, and recommendations for future experimental design.

CHAPTER 2: THEORY

2.1 Multiphase Flow

Methane gas is not readily soluble in water at shallow subsurface pressures and temperatures (Cramer et al, 1999). The fluid dynamics within the pore space therefore consists of multiphase flow of two immiscible fluids, water and methane gas. In the current study we are focused on flow below the water table, such that the pore space is fully saturated with groundwater pre-injection. In order for the gas to be able to move through the pore space it must displace the water that currently resides in the pores. When the two fluids are in contact at a pore throat there is a pressure differential across the interface that connects them. This pressure differential is known as the capillary pressure (Bear, 1972)

$$P_c = P_{nw} - P_w, \tag{2.1}$$

where P_{nw} is the pressure in the nonwetting fluid and P_w is the pressure in the wetting fluid. In our experiment, methane gas is the nonwetting phase and water the wetting phase. Bear (1972) describes the capillary pressure as the tendency of a porous medium to repel the nonwetting phase. The capillary pressure is a function of the size of the pore throat; the smaller the pore throat the greater the capillary pressure. Bear (1972) defines drainage as when a pore space that is initially saturated with the wetting fluid (i.e. water) becomes displaced by the nonwetting fluid (i.e. methane). To facilitate drainage a minimum pressure must be reached in the nonwetting fluid, known as the threshold pressure (Bear, 1972), which is equivalent to the capillary pressure. Threshold pressure is a function of the pore radius and is proportional to the grain size. Leverett (1941) showed that the capillary pressure and hence threshold pressure, is proportional to $1/\sqrt{k}$,

where k is the permeability of the porous medium. Thus, a decrease in permeability results in a commensurate increase to the threshold pressure.

Thomson and Johnson (2000) used an air sparging scenario to put forth a conceptual model of an injected gas plume's evolution (Figure 2.1). Initially, the injection pressure will cause drainage of the pore space around the injection point, as fluid is displaced, and the pores fill with gas. Buoyancy forces then dominate, and the gas begins to flow upwards. When the gas encounters a less permeable layer, and assuming the threshold pressure required to break into that medium has not been achieved, the plume will migrate laterally beneath the less permeable layer. Subsequent upwards migration may only occur at lateral discontinuities in the low permeability layer. This process describes the mechanism for significant lateral migration of the gas plume in a vertically heterogeneous environment.

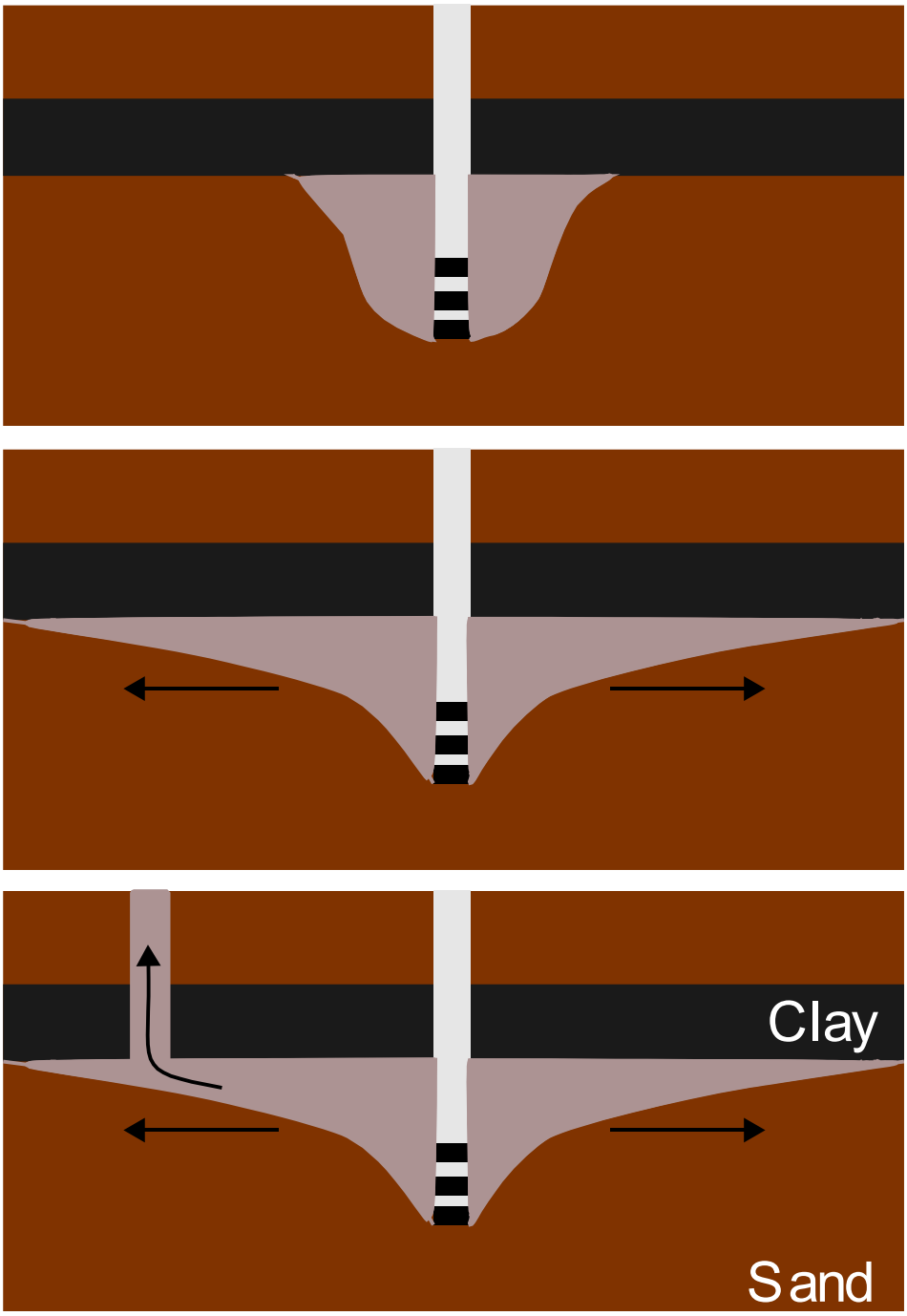

Fig 2.1. Conceptual model of gas plume evolution for a fully saturated confined aquifer. Initially the injection of gas causes drainage around the sparging screen and the gas flows upwards under buoyancy forces (Top). The threshold pressure to enter the less permeable layer (black) is too great and the gas begins lateral migration (Middle). Lateral discontinuities of the less permeable layer provide pathways to surface via buoyancy driven migration (Bottom).

2.2 Electrical Resistivity Methods

Electrical resistivity surveys are used to determine the spatial distribution of subsurface resistivity in a noninvasive and nondestructive manner (Telford, 1990). A known current is applied to the ground across two electrodes and the electric potential measured between two electrodes within the resultant electric field. Having a known current and measured potential allows one to calculate an apparent resistivity at a given location in the subsurface. Subsequently, the apparent resistivity measurements are inverted to create resistivity models of the subsurface. The electrical properties of the subsurface are dependent upon the soil type and pore fluid. The range of resistivities for different minerals and rocks covers many orders of magnitude (Table 2.1), making the method useful for identifying gas in the subsurface.

Material	**Resistivity** $(\boldsymbol{\Omega m})$
Clays	$1 - 100$
Sandstone	$1 - 6.4 \times 10^{8}$
Shales	$20 - 2 \times 10^{3}$
Marls	$3 - 70$
Water (sediments)	$1 - 100$
Oil Sands	$4 - 800$

Table 2.1 Resistivities of different rocks, sediments and water. Adapted from Telford (1990)

2.2.1 Electrical Theory

The resistivity method measures the electric potential difference between two electrodes that arises due to the electric field generated by two current electrodes that apply a continuous direct current into the ground (Figure 2.2). The potential due to a single current point source in a homogeneous space is given by

$$V = \frac{I\rho}{4\pi r}, \tag{2.2}$$

where I is the injected current in Amperes, ρ is the resistivity of the medium in ohm meters, and r is the radial distance from the point source in meters (Telford, 1990). Now, placing this point source on the surface of homogeneous half space, and assuming that air does not permit the flow of current, equation 2.2 becomes

$$V = \frac{I\rho}{2\pi r}. \tag{2.3}$$

The current flows radially away from the electrode creating hemispherical equipotential surfaces beneath the ground-air interface (Telford, 1990). For the field experiment, we introduce a second electrode such that the current flows into the ground via the first electrode and exits via the second. Resulting in two current point sources of equal magnitude and opposite polarity. The updated equation for the potential at a point in the subsurface is given by

$$V_1 + V_2 = \frac{I\rho}{2\pi}\left(\frac{1}{r_1} - \frac{1}{r_2}\right), \tag{2.4}$$

where r_1 is the radial distance from the first electrode and r_2 is the radial distance from the second electrode (Telford, 1990). Electrical resistivity tomography (ERT) uses the potential difference between a pair of potential electrodes which leads to

$$\Delta V = \frac{I\rho}{2\pi}\left[\left(\frac{1}{r_{AM}} - \frac{1}{r_{BM}}\right) - \left(\frac{1}{r_{AN}} - \frac{1}{r_{BN}}\right)\right], \tag{2.5}$$

where r_{ij} are the radial distances between the current electrode i to the potential electrode j, and ΔV is the potential difference between the two potential electrodes (Figure 2.2). As the spacing between the electrodes increases, the survey probes deeper into the subsurface. The measured values of potential and injected current, together with the electrode configurations of the measurements are used in an inversion scheme to estimate a model of the subsurface resistivity structure (Chapter 4).

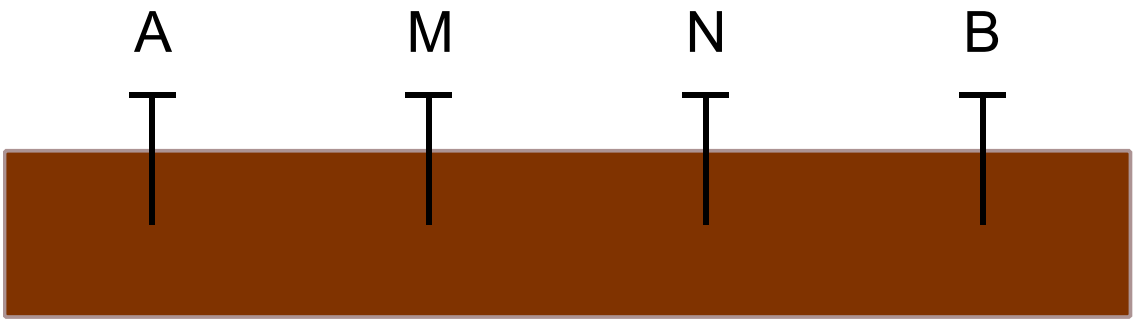

Fig. 2.2 Schematic showing the set up for a general resistivity array where A and B are the current electrodes and M and N are the potential electrodes.

The electrical conductivity (inverse of resistivity, $\sigma = \frac{1}{\rho}$) of a fully or partially saturated sandy soil can be estimated via Archie's Law (Archie, 1942):

$$\sigma = \frac{\phi^m S_w^n}{a}\sigma_w, \tag{2.7}$$

where σ is the conductivity of the soil (S/m), S_w is the water saturation, ϕ is the porosity of the soil, and σ_w is the conductivity of the pore fluid. a, m, and n are empirically derived parameters where a is the tortuosity factor, m is the cementation exponent, and n is the saturation exponent. The Archie model shows that as the gas displaces the groundwater in the pore space the water saturation will decrease, resulting in a lower conductivity and hence a higher resistivity.

This relationship breaks down when a there are a high percentage of clay grains in the soil. The clay minerals permit the conduction of current along the clay surface and so need to be accounted for (Mavko et al, 2009). One model for conductivity in clay rich sediments is the Waxman-Smits model (Ramirez et al., 1993):

$$\rho_{tot} = \frac{(\phi S_w)^{-\nu}\rho_w}{1+\rho_w B Q_{vb}(\phi S_w)^{-1}}, \tag{2.8}$$

where ρ_{tot} is the resistivity of the partially saturated sediment $(\Omega\ cm)$, ν is the combined saturation exponent (~2), ρ_w is the resistivity of the pore fluid, B is the equivalent conductance of the exchangeable cations, and Q_{vb} is the cation exchange capacity of the clay. Similar to the Archie model, the Waxman-Smits model shows that a decrease in water saturation will result in an increase in resistivity.

2.2.2 Data Acquisition

Two array types were used in this field experiment, the dipole-dipole array and the gradient array. The dipole-dipole array set up is shown in Figure 2.3. The current electrodes (C1 and C2) are paired together and separated by a distance a, as are the potential electrodes (P1 and P2). The two pairs are then separated by an integer multiple of the electrode separation, na, where n is an integer and is referred to as the expansion factor (Telford, 1990).

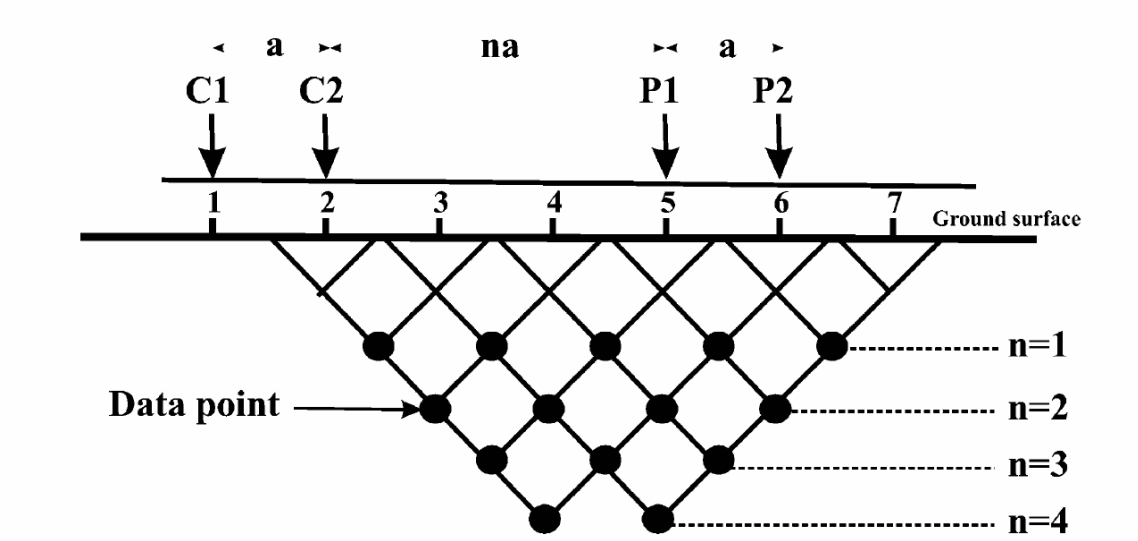

Fig. 2.3. Dipole-dipole array set up for field acquisition. C1 and C2 are the current electrodes, P1 and P2 are the potential electrodes. The separation of the electrode pair is a multiple n of the electrode spacing a. The data points below show how the acquired data map to data levels depending on the expansion factor n. (Adepelumi et al, 2006)

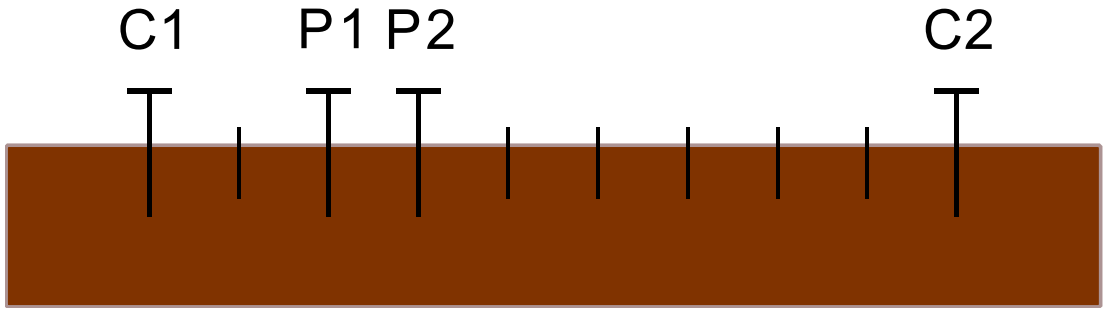

Fig. 2.4. Gradient array geometry. The current electrodes, C1 and C2, are kept at the ends of the survey. Each combination of potential electrode locations, P1 and P2, between the current electrodes are activated when recording data.

The gradient array set up is shown in Figure 2.4. In this configuration, the two current electrodes, C1 and C2, are located at either ends of the array. Potential electrodes are moved to each combination of locations between the current electrodes to take a measurement. Combining

the two data sets increases our density of measurements in the zone of interest, with the aim of reducing the effects of erroneous measurements.

2.3 Distributed Temperature Sensing

Electrical current in sedimentary structures flows through the pore fluid and by surface conduction on the grain surfaces (Hayley et al, 2007). Differences in conductivity due to temperature are also caused by changes in viscosity in the pore fluid and ionic mobility at the grain surface (Hayley et al, 2007). Hayley et al (2007), conducted a laboratory experiment on glacial till samples and observed that from 0-25°C, conductivity increases linearly with temperature. Consequently, a temperature profile of the subsurface must be obtained to adjust the data for the effects of temperature.

Distributed temperature sensing (DTS) is a method for collecting subsurface temperature data that utilizes fiber optic cables. The entire length of the fiber is capable of sensing temperature variations, enabling continuous temperature assessment, and a considerable improvement as compared to single point measurements. The DTS used in this experiment relies on the Raman scattering effect (Rogers, 1991), which is a quantum mechanical phenomenon. Molecules within the silica fiber are vibrating depending on their temperature. A photon that is travelling down the fiber may be absorbed by a molecule, which raises the energy state of the molecule to a more excited state. The molecule will then spontaneously drop to a lower energy state, re-emitting a photon. If the molecule is already in an excited state, as a result of having a higher temperature, the re-emitted photon can have greater energy than the photon that was originally absorbed by the molecule. Hence, the re-emitted photon will have a shorter

wavelength (Rogers, 1991), and these re-emitted photons are the anti-Stokes part of Raman scattering. There is also a temperature independent contribution to Raman scattering known as Stokes scattering, which is where the remitted photon has less energy than the absorbed photon. The optical fiber is connected to an interrogator that pulses laser light down the fiber and records the backscattered light. By analyzing the intensities of the Stokes and anti-Stokes backscattered light, a temperature profile along the fiber is generated (Hwang et al., 2010). Given the constant velocity of light in the optical fiber, the localization of the temperature measurement can be calculated from the travel time between sending the pulse and the recording of backscattered light.

2.4 Biodegradation of Methane

Methane gas and other hydrocarbons can undergo physical and chemical alterations in-situ due to biodegradation by microorganisms that are resident in the subsurface (Atekwana et al, 2004). There are field examples of increased conductivity in areas of hydrocarbon contamination thought to be due to biodegradation (e.g. Atekwana et al., 2000 and 2002). Sauck (2000) attributed the higher bulk conductivities to an increase in the total dissolved solids (TDS) in the groundwater. The mechanism begins with the degradation of hydrocarbons, producing acids, which weathers the minerals in the surrounding sediment, thus causing an increase in TDS. Increases in conductivity are likely in and below areas of high biodegradation (Sauck, 2000). Oxygen rich waters offer the best conditions for biodegradation (Sauck, 2000), which tends to be in areas of groundwater recharge. This leads to the development of long thin high conductivity plumes at the top of the dissolved hydrocarbon plume.

2.5 Review on Electrical Resistivity Monitoring of Multiphase Flow

Electrical resistivity methods have long been used for identifying and monitoring solutes and free phase gas in the subsurface. The applications range from mapping salt water intrusion (Nguyen et al., 2009), monitoring contaminants from landfills (e.g. Rosquist et al., 2011, Rosquist et al., 2011-2), air sparging (Lundegard and Labreque, 1995 & 1998), monitoring methane gas production in peatlands (e.g. Slater et al.,2007; Terry et al., 2016), and monitoring carbon dioxide during sequestration experiments (Schmidt-Hattenberger et al., 2013). These experiments have proven the efficacy of ERT as a viable method for long term monitoring and time-lapse analysis of changes in the position of gases and solutes in the near surface.

2.5.1 Air Sparging

Air sparging is a method of groundwater remediation in areas of contamination that became common in the 90's (Lundegard and Labreque, 1995). The method enhances the remediation of some contaminants by either contaminant partitioning into the vapor phase or increased biodegradation due to the introduction of oxygen into the subsurface (Lundegard and Labreque, 1995). Knowledge of the movement of the gas plume can be gained by ERT methods and is necessary to target the areas of contamination efficiently.

Lundegard and Labreque conducted multiple air sparging experiments in homogeneous sand aquifers (Lundegard and Labreque, 1995) and highly heterogenous glacial till environments (Lundegard and Labreque, 1998). Of particular interest to this investigation are their findings

from a cross hole ERT experiment in 1998, in which air was injected into a fully saturated glacial till environment. Their results show that the migration pathways of the gas in the heterogenous environment were more complex when compared to the homogeneous environment. The plume moved predominantly laterally from the sparging screen suggesting a less permeable confining layer was trapping the gas. Over time their data showed increases in resistivity above the confining layer suggesting the air was slowly leaking through the low permeability layer.

2.5.2 Dense Nonaqueous Phase Liquid

Dense nonaqueous phase liquids (DNAPLs) are a common form of groundwater contamination consisting of coal tars, chlorinated solvents, creosote and polychlorinated biphenyl oils (Brewster et al., 1995). These liquids have a greater density than ground water and have a low solubility allowing them to flow through the groundwater, predominantly under the force of gravity. Hence, the general flow is vertically downwards. DNAPLs are analogous to free phase gas, but they operate in the opposite direction. Therefore, when meeting a low permeability layer in the subsurface, DNAPLs will spread laterally (Brewster et al., 1995).

Most of the literature covers the remediation of DNAPLs and the subsequent decrease in resistivity as the DNAPL is subsequently removed. Daily and Ramirez (1995) performed a laboratory experiment of a DNAPL leak using ERT to monitor the changes. They showed that DNAPLs cause an increase in resistivity as the liquid displaces water within the pore space. Newmark et al. (1998) monitored the removal DNAPL using cross hole ERT, noting a reduction in resistivity as pumping began, likely due to the removal of the DNAPL. Their findings suggest that the DNAPL followed the path along the top of a low permeability layer before being

removed by the pumping well, implying that geologic variations of permeability within the subsurface control the preferential pathways of DNAPL flow.

2.5.3 Carbon Dioxide

With the growing concern of climate change and the role that carbon dioxide plays in the warming of the Earth; carbon capture and storage is becoming ever more popular and increasingly necessary as part of a global CO_2 reduction plan. Carbon sequestration is the act of injecting CO_2 in liquid form into deep brine aquifers with the hope that it remains there for 100s to 1000s of years (Lal, 2008). Geophysical methods have been utilized to examine whether the CO_2 is remaining within the aquifer and to track the movement of the plume through time.

Schmidt-Hattenberger et al. (2013) deployed a multi-disciplinary monitoring strategy to detect the extent of a CO_2 plume in a saline aquifer. A permanent array of surface and downhole electrodes were installed to provide frequent acquisitions of ERT data. The results highlight the suitability of permanent electrode arrays as a method of subsurface monitoring for changes in pore fluid. Schmidt-Hattenberger et al. (2013) further highlight the extended benefit of detecting the movement of brine water into overlying freshwater aquifers due to displacement by CO_2.

Auken et al. (2013) utilized a 320-electrode 3D ERT array to monitor dissolved CO_2 migration in a shallow subsurface setting. In their study, CO_2 was injected at 5 and 10 m depth and time lapse ERT inversions imaged a decrease in resistivity due to the dissolved plume of CO_2 over 120 days. Over this time the dissolved plume migrated 25m in the direction of groundwater flow. ERT proved useful in outlining the plume's shape as well as providing a

wider scope of imaging as compared to the discrete spatial measurements provided by screened borehole monitoring.

2.5.4 Methane Gas

The majority of studies focused on methane gas monitoring have focused on biogenic sources such as peatlands (e.g. Slater et al., 2007; Terry et al., 2016), or anthropogenic sources such as landfills (e.g. Rosquist et al., 2011, Rosquist et al., 2011-2). These sources do not originate from a single point, but rather the large-scale decomposition of organic material. The release of gas into the surrounding soil displaces the resident pore water, resulting in an increase in resistivity.

In a study that acts as a precursor to the subject of this thesis, Steelman et al. (2017) used time-lapse ERT to monitor the evolution and fate of an injected methane gas plume in a near surface sandy unconfined aquifer. In that study, 51.35 m^3 of methane was injected at depths of 4.5 and 9 m over a 72-day period. The time-lapse ERT inversions revealed changes in resistivity of up to 30% around the upper injection zone, and evidence of smaller plumes, disconnected from the main plume, migrating horizontally. The aquifer was homogenous and so migration pathways were relatively simple. The gas migrated mostly vertically, followed by migration in the groundwater flow direction.

CHAPTER 3: FIELD SITE AND EXPERIMENTAL DESIGN

3.1 Local Geology

The field experiment was conducted at the University of British Columbia's Energy and Environment Research Initiative (EERI) field research station near the town of Hudson's Hope in North-East British Columbia, Canada. The site is located on the bluffs of the Peace River and is underlain by glacial and interglacial deposits from the Quaternary period. The Peace River Valley comprises a mixture of glacial till deposits from the Laurentian and Cordilleran ice sheets, and fluvial sediments, likely deposited during interglacial periods (Hartman and Clague, 2008). As a result of the depositional history, the site exhibits a significant amount of vertical and lateral heterogeneity within the near surface in the area of the experiment. The late Cretaceous sedimentary bedrock ranges from between 15 m below surface at the valley floor to 180 m below surface at higher elevations (Hartman and Clague, 2008). Consequently, with our site located >100m above the river valley, the bedrock is not encountered in the experimental injection, which is focused at depths 30 m below ground surface and above, assuming vertical migration. Based on the water level of wells installed at the site, the interpreted groundwater direction across the site is from Northwest to Southeast.

3.2 Extracted Core and Geophysical Logging

Core descriptions obtained from monitoring wells installed throughout the site confirm that the near surface is a mixture of glacial till and fluvial deposits (Figure 3.2). The upper layer

of sediment is comprised of clay and silt diamict to a depth of 11 m, which acts as a confining layer to the predominantly sandy aquifer beneath the discontinuous confining layer. The aquifer section is a 15m thick package of interbedded fine-grained sands to silts and silty clays to approximately 26 m depth. There is significant lateral and vertical heterogeneity within this sandy zone; the core logs show thin clay/silt layers within the predominantly sand filled zone of the aquifer. The fine-grained sand package is underlain by clay to silty clay. The core is moderately sorted within each section and contains many pebbles and cobbles throughout (between 1-10%).

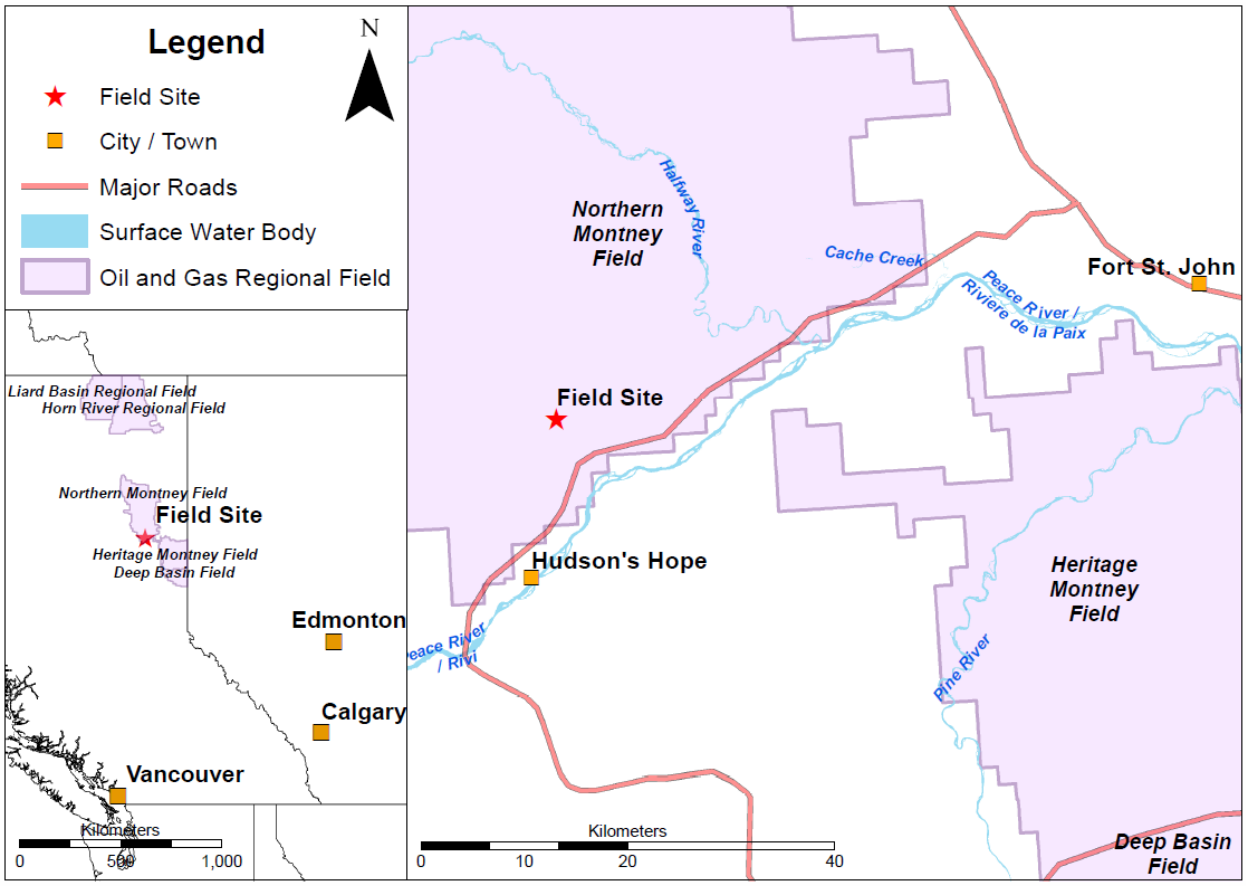

Map Projection: NAD 1983 BC Environment Albers (WKID 3005)
Oil and Gas Regional Fields retrieved from British Coloumbia Data Catalogue, March 2019: http://catalogue.data.gov.bc.ca
Base map features (cities, roads, waterways, boarders) retrieved from Government of Canada Open Data, March 2019: https://open.canada.ca/en/open-data
American Border Polygons retrieved from United States Census Bureau, March 2019: https://www.census.gov/geo/maps-data/data/tiger-cart-boundary.html

Fig. 3.1. Map of western Canada highlighting the location of the field research site.

The site has little to no elevation change (<1.6 m across the area of investigation) and is fully saturated below 3 m below ground surface (bgs). The water table decreased by approximately 30-50 cm from the NW well PW1 to the SE well PW4, indicating a NW to SE groundwater flow direction.

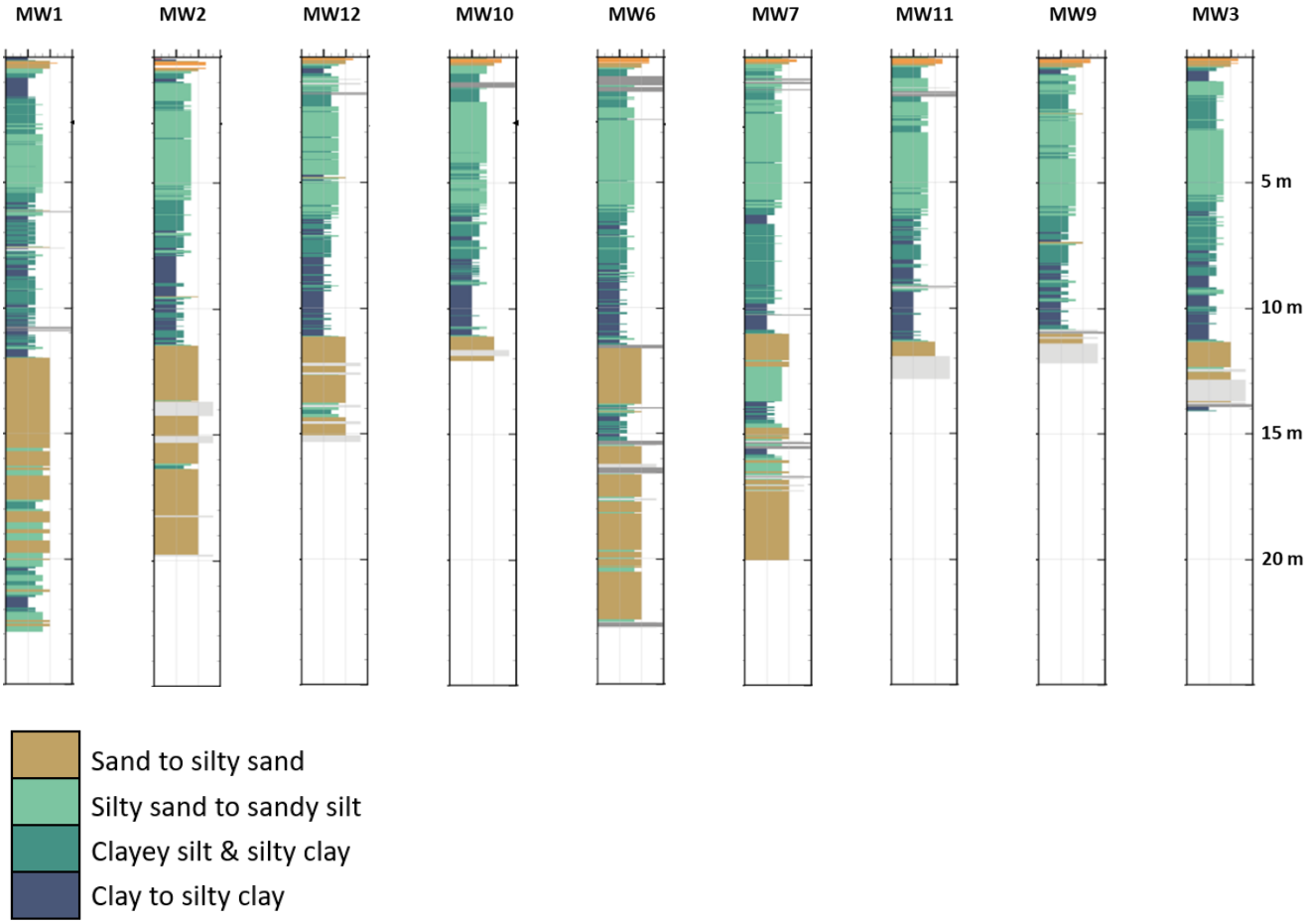

Fig. 3.2. Interpreted core logs show an ~11 m thick clay/silt layer above the sandy aquifer. There is also evidence of clay/silt layers within the sand aquifer which may act as baffles to the upward migration of gas (Image courtesy of Jessie Chao).

Gamma, neutron porosity, and resistivity logging were conducted in the location of PW1 bgs to a depth of 70 m and the interpreted well logs are shown in Figure 3.3. The dashed lines show the interpreted layer boundaries. Layer A ranges from 0 - 4.5 m and is comprised of heterogeneous clayey silt diamict. This layer is characterized by high gamma counts of 75-105 API and a resistivity of approximately 10 Ωm. Layer B ranges from 4.5 - 12 m and is clayey to silty diamict, characterized by gamma counts of approximately 60 API and resistivity on the order of 60 Ωm. Importantly, layers A and B are interpreted to act as an impermeable seal to the confined aquifer below. Beneath the confining layer, layer C extends from 12 - 23 m depth and is comprised of fine sand to silty diamict. This layer is characterized by gamma counts of approximately 45 API and resistivity on the order of 70-80 Ωm and represents the main aquifer interval. Layer D ranges from 23 - 26 m and contains pebbly fine sand. This layer is characterized by gamma counts of approximately 40 API, a strong drop in the neutron porosity count, and variable resistivity between 30-100 Ωm. Layer E ranges from 26 - 61 m and is comprised of silty, clay diamict. This layer is characterized by gamma counts of 75 API and a resistivity between 10 and 20 Ωm.

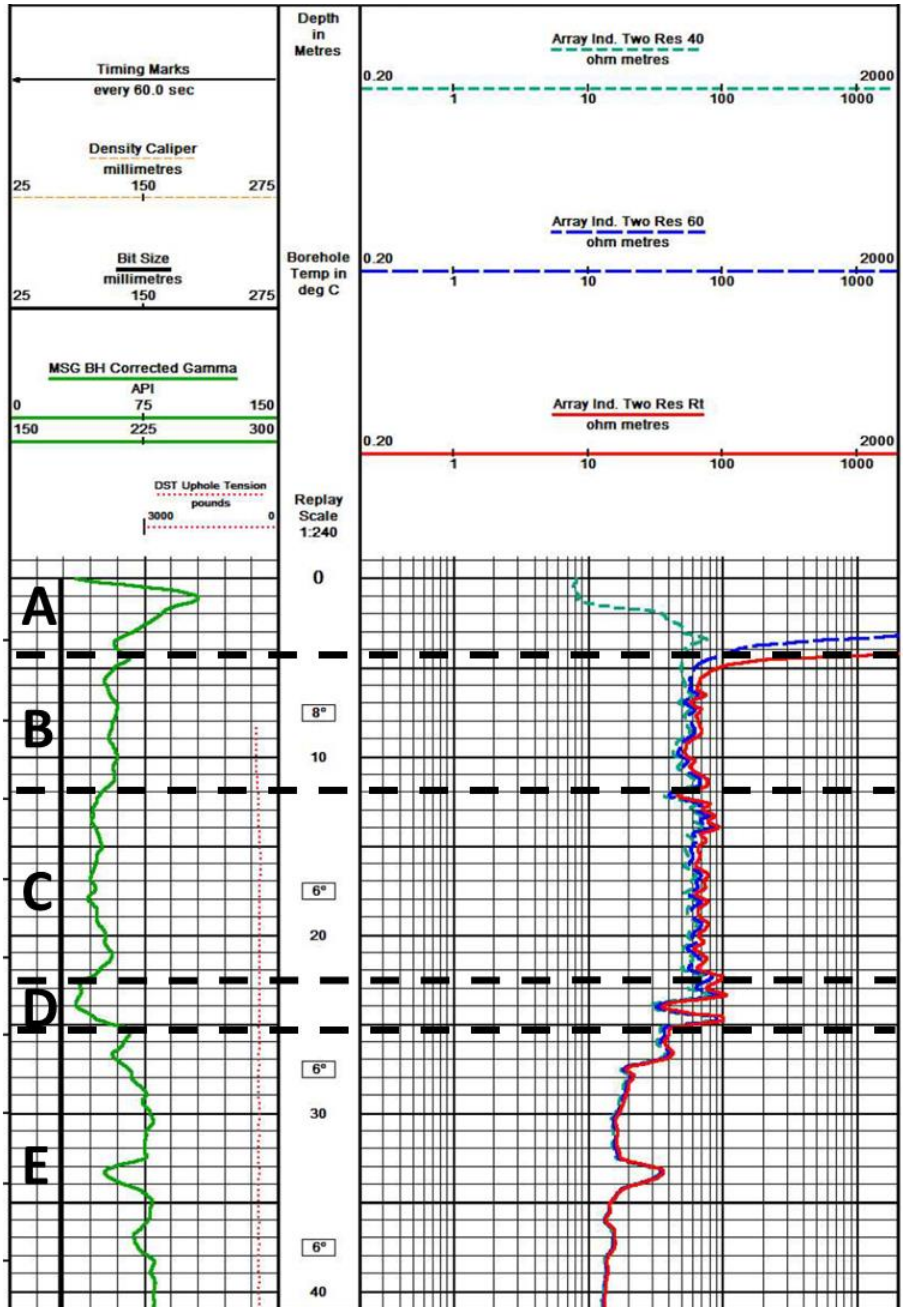

Fig. 3.2. Geophysical well logs from PW1. Dashed lines show interpreted layers. A (0 - 4.5 m): Soils to heterogeneous clayey silt diamict. Characterized by high gamma counts of 75-105 API. Resistivity on the order of 10 Ω-m. B (4.5 – 12 m): Clayey to silty diamict. Characterized by gamma of approximately 60 API and resistivity on the order of 60 Ω-m. C (12 – 23 m): Fine sand, silty diamict. Characterized by approximately 45 API and resistivity on the order of 70-80 Ω-m. D (23 – 26 m): Pebbly fine sand. Characterized by approximately 40 API, a strong drop in the neutron count and variable resistivity between 30-100 Ω-m. E (26 – 61 m): Silty, clay diamict: Characterized by gamma of 75 API and a resistivity between 10 and 20 Ω-m.

3.3 Injection Design

The injection target is at the base of the confined interbedded fine-grained sand and silt aquifer at 26 m bgs. A single screened injection well bore was drilled at a 45° angle to vertical in a NE-SW orientation, orthogonal to the expected groundwater flow direction. The well bore extends to a total vertical depth of 26 m bgs(Figure 3.3), where the injection occured. An 85% methane composite gas mixture was injected at the field site, designed to match the natural gas composition of the Montney resource play (Table 3.1). The injection lasted for 66 days between June 12th and August 16th, 2018 with a constant injection rate of 1.5 m^3 per day for a total of 97.662 m^3. The injection location was selected to allow upward migration of the gas through the sandy aquifer.

Gas	**C_1**	**C_2**	**C_3**	**$>C_4$**	**CO_2**	**N_2**	**He**
Typical Montney Gas	0.85	0.08	0.03	0.02	0.001	0.002	0.0001
EERI Synthetic Montney Gas	0.85	0.08	0.05	0	0.01	0.005	0.005

Table 3.1. Composition of Montney gas and synthetic gas used for the experiment (Adapted from Cahill et al., 2019).

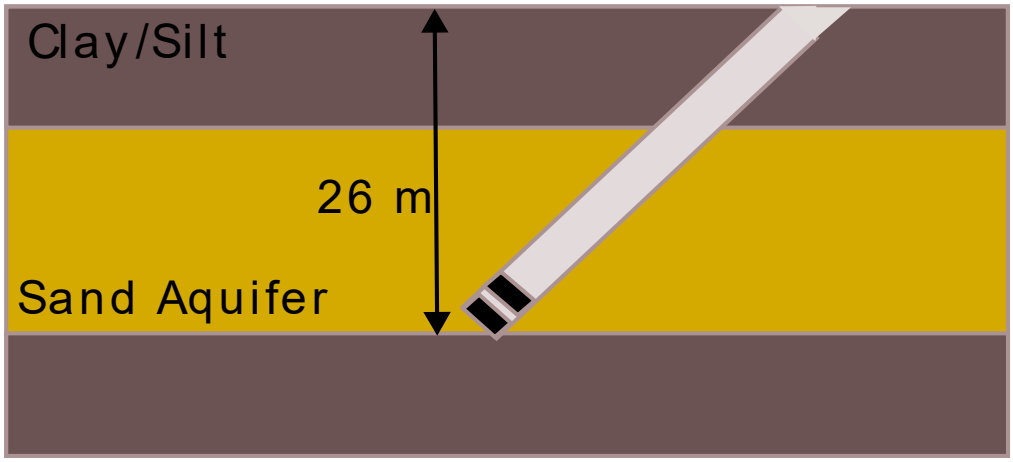

Fig. 3.3. Cross-sectional schematic of injection wellbore with sparging screen. The well was drilled to target the base of the sand aquifer at 26 m depth. The aquifer is sealed by approximately 12 m of clay/silt diamict. The grey layers indicate clay and silt dominated matrix and the yellow layer represents the fine-grained sand aquifer.

3.4. Electrical Resistivity Tomography Surveys

To ensure repeatable results for time-lapse imaging, three ERT lines were permanently installed with 81 12" electrodes per line. The three lines are indicated in Figure 3.4, which include two NW-SE lines that cross the injection location indicated from A to B and C to D, with an orientation selected to match the interpreted groundwater flow direction. The two lines are differentiated by their electrode spacing, where Line 1 from A-B has 5 m electrode spacing and Line 1 from C-D has 2.5 m electrode spacing. The wider spacing Line 1 provides a greater depth of investigation, whereas the 2.5 m electrode spacing provides greater resolution in the immediate near surface surrounding the injection. Line 3 runs from E to F in a SW-NE orientation and utilizes a 2.5 m electrode spacing. Line 3 intersects Line 1 at the observation well PW5, which lies at the center of Line 3 and 8 m downgradient from the injection location along

Line 1. The injection point lies at the center of the 2.5 m spacing Line 1 and is 20 m to the northwest of the center of the Line 1 from A-B.

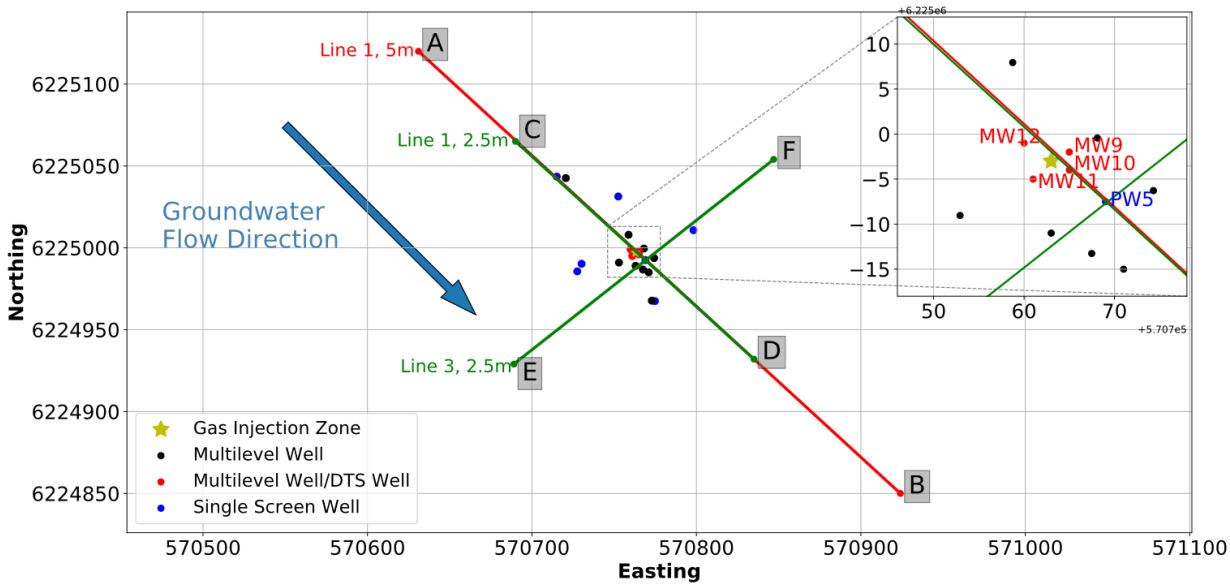

Fig. 3.4. Site map for methane gas injection showing the three ERT lines AB, CD, EF. The injection is located at the center of line CD. Wells MW9, MW10, MW11, and MW12 contain optical fiber for DTS measurements.

The time series of ERT data profiles were collected with the ABEM Terrameter LS 2 during six site visits pre and post injection from June 5th to September 9th (Figure 3.5), with injection discontinued on day 65. Line 1 (2.5 m and 5 m spacings) had data collected 9, 23, 49, 61, and 88 days after the start of injection and Line 3 had data collected 9, 22, 49, 62, and 89 days after the start of injection. A gradient array and a dipole-dipole array were used to image all of the profile lines in the experiment. The dipole-dipole and gradient surveys contained 1469 and 1478 measurements respectively and each individual data set took approximately 30 minutes to collect. During data collection, between two and four repeats of each measurement were stacked

and averaged, and the instrument advanced to the next measurement if the standard deviation between these measurements was < 2.5%.

The weather throughout the injection was primarily hot and dry, although interrupted by infrequent high intensity rainfall events, meaning the very near surface was often partially unsaturated. The water level varied from 2.37 m to 2.97 m bgs in PW1 over the course of the monitoring period. The surveys of June 6th and September 8th and 9th were conducted during light rain, although, given the very low permeability of the clay in the near surface, we assume the near surface saturation conditions were similar to those in previous surveys.

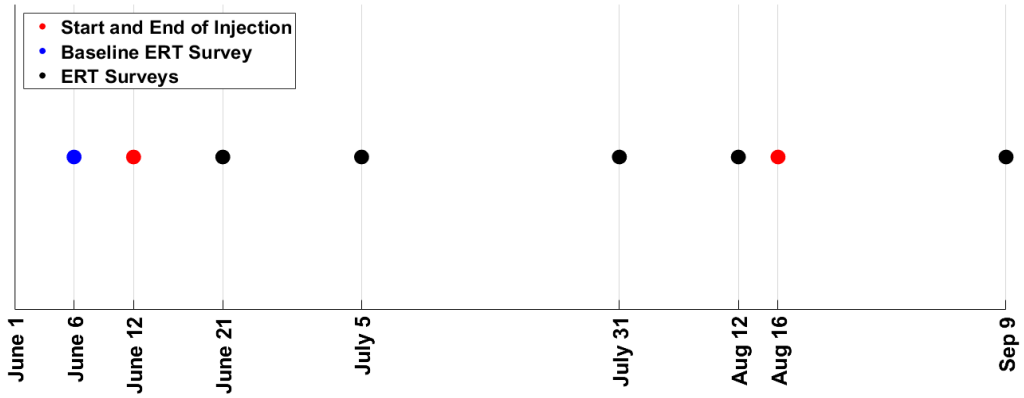

Fig. 3.5. Timeline for data collection and injection period.

3.5. Distributed Temperature Sensing Installation

Optical fiber for DTS measurements was installed downhole in four of the monitoring wells surrounding the injection location: MW9, MW10, MW11, and MW12 (Figure 3.4). The depths of the wells are 21.34 m, 20.73 m, 20.88 m, and 20.73 m respectively. 2” diameter PVC pipe was installed into the borehole for the depth of the hole, and the fiber was attached to metal

spacers that were clamped to the PVC every 4 m to keep the fiber next to the borehole wall (Figure 3.6). This was essential to keep the fiber thermally coupled to the formation. The boreholes were then backfilled with bentonite and one-foot sections of sand around the monitoring screens that were placed at the bottom of each borehole as well as at 2, 4, and 8 m from the bottom of the hole. The individual fiber loops for each well were installed separately and then fusion spliced together to form one large loop. The interrogator was installed on June 6th by Silixa and recorded measurements every hour until it was demobilized from the site on August 13th. The fiber had a spatial sampling interval of 0.25 m and each data recording represents the average temperature over a 15-minute period.

Fig. 3.6. Photograph showing how the DTS fiber was attached to the metal spacers to keep it flush with the borehole wall. This was done to ensure optimal thermal coupling with the surrounding formations.

3.6 Expected Behavior of Injected Gas

As evidenced by the core logs, there are many silt/clay beds that are likely limited in their lateral continuity within the aquifer zone. Given the highly heterogeneous nature of the aquifer, a complex migration pathway is anticipated, such that the layers of clays and silts within the aquifer may act to baffle the upwards, buoyancy driven, flow of the gas. As a result, there is the potential at this site for considerable lateral migration either before vertical flow is seen or after a few meters of vertical flow. The upper layer of 11 m thick clay and silt are expected to confine any gas within the aquifer and prevent gas from migrating into the vadose zone and ultimately into the atmosphere. Accordingly, gas detection at the surface is estimated to be minimal. Based on the results of Klazinga (2018) and Lundegard and Labreque (1998), it is likely that any gas that does migrate to the top of the aquifer will form a thin layer with large lateral extent beneath the clay/silt confining layer. Furthermore, given the very low permeability of the clay diamict and the insoluble nature of methane gas, the gas may remain in-situ for years. However, the numerous monitoring wells onsite, despite being backfilled with bentonite, offer potential vertical pathways to surface.

The results of the Lundegard and LaBrecque (1998) air sparge experiment in a highly heterogeneous glacial till environment can provide useful insights to our experiment. Their results show significant lateral migration and a trapping of the plume below an assumed low permeability layer that was located just above the injection screen. Numerical modelling by Klazinga (2018) shows that the groundwater flow direction has some influence on the direction of the plume migration during buoyancy driven flow. We anticipate that the plume will ultimately rise on the downgradient side of the injection due to the influence of groundwater

flow, but once lateral migration occurs beneath a low permeability layer, the migration direction is unpredictable without detailed knowledge of the overlying permeability structure. The gas should migrate up dip. However, the local geology during deposition of the fluvial sediment likely means that there is a highly channelized system, where subtle variations in permeability will direct the migration of gas. The gas saturation within the pore space should increase as more gas is injected into the aquifer, resulting in a higher resistivity, as gas displaces the pore fluid. Consequently, we anticipate that the resistivity differences, relative to pre-injection values will increase in magnitude over the course of injection. Similarly, we might expect that the data post injection begins to return to the background data as there is no new influx of gas and the injected gas may have migrated outside the zone of investigation.

CHAPTER 4: TIME-LAPSE INVERSION

4.1. Data Processing

The data files were exported from the ABEM LS2 Terrameter in a RES2DINV format (.dat) indicating the electrode positions and a recorded resistance. To remove erroneous data from the files, the data were loaded into RES2DINV v 3.54.57 (Loke, 2002). The *edit bad datum points* function was utilized to remove notably erroneous data points, based on extreme values with no adjacent anomalous response. A first pass inversion using the RES2DINV software was then performed to identify areas in the data that needed to be further refined. The RES2DINV functionality for removing data points with a high RMS error was then used to trim any data with RMS error over 50%. The two edited data sets from each time series, i.e. the gradient and dipole-dipole data, were then combined into a single data set for each of the orthogonal transects. The background data sets of Line 1 2.5 m and Line 3, and the July 5th data set of Line 1 2.5 m did not require any edits. The August 12th, 13th, and the September 8th, and 9th surveys recorded anomalous resistivities associated with a poor electrode contact on one of the cables. The issue could not be resolved in the field. These data were edited to remove anomalous values, however, inversion artifacts still remain for these data sets.

4.2. Data Inversion

The following section outlines the electrical resistivity inversion scheme starting from the forward problem, moving on to inversion theory, and concluding with the implementation of the methodology using an open source Python package, SimPEG.

4.2.1. The Forward Problem

At the foundation of the inversion procedure we are required to forward model the electric field produced by a pair of electrodes, in response to a given subsurface resistivity distribution. Forward modelling produces a data estimate for the current model being tested that we can compare to the measured data obtained at the field site.

Electrical resistivity tomography experiments measure voltages in response to a known input current. The measurements recorded are determined by the distribution of conductivity within the subsurface, and the governing equation for this relationship is as follows (Pidlisecky, 2007):

$$\nabla \cdot (-\sigma \nabla \phi) = I\big(\delta(\boldsymbol{r} - \boldsymbol{r}_{s^+}) - \delta(\boldsymbol{r} - \boldsymbol{r}_{s^-})\big), \tag{4.1}$$

Where ∇ is the gradient operator, $\nabla \cdot$ is the divergence, σ is the conductivity (inverse of resistivity), ϕ is the potential field, I is the current, $\boldsymbol{r}_{s^+}$ and $\boldsymbol{r}_{s^-}$ are the positive and negative current source locations, and $\delta(\boldsymbol{r} - \boldsymbol{r}_s)$ is the Dirac delta function centered on the location of the current source. This problem is solved in the Fourier domain for a discretized model space using numerical methods, e.g. Gauss-Newton, as outlined in Pidlisecky (2008).

Having a value for the field in the model space allows one to calculate the value of a measurement for a given array geometry and create an array of data estimates, $\boldsymbol{d}_{est}$.

4.2.2. Inverse Theory

The objective function to be minimized during the ERT inversion used here is comprised of a data misfit function and a regularization norm. The data misfit term is as follows for an l2-norm:

$$\phi_d(\boldsymbol{m}) = \frac{1}{2}\|\boldsymbol{W_d}(F(\boldsymbol{m}) - \boldsymbol{d}_{obs})\|_2^2, \tag{4.2}$$

where $F(\boldsymbol{m})$ encompasses the forward modeling of the governing equations to produce a predicted data set $\boldsymbol{d_{est}}$, $\boldsymbol{d}_{obs}$ is the observed data in the field, and $\boldsymbol{W_d}$ is a diagonal weighting matrix with elements $\boldsymbol{W_{d_{ii}}} = \frac{1}{\varepsilon_i}$, where ε_i is the estimated standard deviation of the i^{th} data point (Cockett et al., 2015). ε_i is comprised of $\varepsilon_i = floor + \%|d_i|$, where the percentage term stabilizes the inversion when there are a large range of data values and the $floor$ provides stability if there are data close to zero (Cockett et al., 2015). The regularization norm is given by the expression

$$\phi_m(\boldsymbol{m}) = \frac{1}{2}\left\|\boldsymbol{W_m}\left(\boldsymbol{m} - \boldsymbol{m}_{ref}\right)\right\|_2^2, \tag{4.3}$$

where $\boldsymbol{m}_{ref}$ is a reference model, commonly a homogeneous half space with a resistivity close to the expected value of the investigation area, and $\boldsymbol{W_m}$ is the regularization matrix and is a combination of the matrices for smallness and first order smoothness in the x and z directions

$$\boldsymbol{W_m} = [\alpha_s \boldsymbol{I},\ \alpha_x \boldsymbol{W}_x^T,\ \alpha_z \boldsymbol{W}_z^T\ ]^T, \tag{4.4}$$

where the α_s is a scalar that penalizes differences between the model and the reference model, $\boldsymbol{W}_x^T$ and $\boldsymbol{W}_z^T$ are the discretized gradient operators in the x and z directions, and α_x and α_z are scalars that determine smoothing in the x and z directions. The two misfit terms are combined to form our final objective function to be minimized:

$$\phi(\boldsymbol{m}) = \phi_d(\boldsymbol{m}) + \beta\phi_m(\boldsymbol{m}). \tag{4.5}$$

β is the regularization parameter that balances the data misfit and the model regularization and is either set as a constant or determined by a cooling method, whereby, we start with a large value and iteratively reduce β until the tolerance criteria are met (Cockett et al., 2015).

If we take the gradient of the objective function in equation 4.5, we produce the term

$$g(\boldsymbol{m}) = \boldsymbol{J}(\boldsymbol{m})^T \boldsymbol{W_d^T W_d}(\boldsymbol{F}(\boldsymbol{m}) - \boldsymbol{d_{obs}}) + \beta \boldsymbol{W_m^T W_m}\big(\boldsymbol{m} - \boldsymbol{m_{ref}}\big), \tag{4.6}$$

where $\boldsymbol{J} = \boldsymbol{\partial d_{est}/\partial m}$ is the sensitivity (Jacobian) matrix. A Taylor expansion of $\boldsymbol{F}(\boldsymbol{m})$ about a small perturbation in the model $\delta\boldsymbol{m}$ results in

$$\boldsymbol{F}(\boldsymbol{m}^k + \delta\boldsymbol{m}) \approx \boldsymbol{F}(\boldsymbol{m}^k) + \boldsymbol{J}(\boldsymbol{m}^k)\delta\boldsymbol{m}, \tag{4.7}$$

where k is the iteration number and $\boldsymbol{m}^k$ is the starting model for that iteration (Cockett et al., 2015). Hence, we can solve for the perturbation $\delta\boldsymbol{m}$ by

$$(\boldsymbol{J}(\boldsymbol{m})^T \boldsymbol{W_d^T W_d J}(\boldsymbol{m}) + \beta \boldsymbol{W_m^T W_m})\delta\boldsymbol{m} = -g(\boldsymbol{m}). \tag{4.8}$$

Subsequently, the updated model is given by:

$$\boldsymbol{m}^{k+1} = \boldsymbol{m}^k + \gamma\delta\boldsymbol{m}, \tag{4.9}$$

where γ is found via a line search and is between 0 and 1 (Cockett et al., 2015). The system of equations in equation 4.8 can be solved using various optimization techniques. In our study we have utilized SimPEG's inexact Gauss-Newton method. The routine is iterated until the stopping criteria are met or the maximum number of iterations are completed to produce a final model estimate.

4.2.3 SimPEG

All the inversions presented here were produced using SimPEG, an open source framework for simulation and inversion of geophysical problems coded in Python. A detailed description of the functionality and methodology can be found in Cockett et al. (2015), and the workflow of the inversion procedure will be introduced in Section 4.2.3.1 and is shown in Figure 4.1.

4.2.3.1 Mesh Design

A central component of the inversion scheme is the discretization of the model onto which the governing equations are implemented. SimPEG utilizes a node centered, staggered grid, mimetic finite volume discretization (Cockett et al, 2015), and the size of the cells and the extent of the grid are determined by the input data set. For our data, the cell size allocated allows for two grid cells per dipole spacing (e.g. 1.25 m cell for dipole separation of 2.5 m). To reduce the interference of boundary effects, the edges of the grid are variably padded to move the boundaries away from the area of investigation. For this reason, there are seven cells either side and below the active model, which corresponds to the area of the model for which SimPEG will calculate resistivity values, with cell widths increasing by a factor of 1.3 per cell, resulting in the total model cells for Line 1 2.5 m and Line 3 being 18540 (Figure 4.2) and Line 1 5 m having 13320 cells (Figure 4.3). The mesh produced from the background data set is then used for all subsequent time series data sets. Once the mesh has been generated it is passed into the inversion initialization (Figure 4.1).

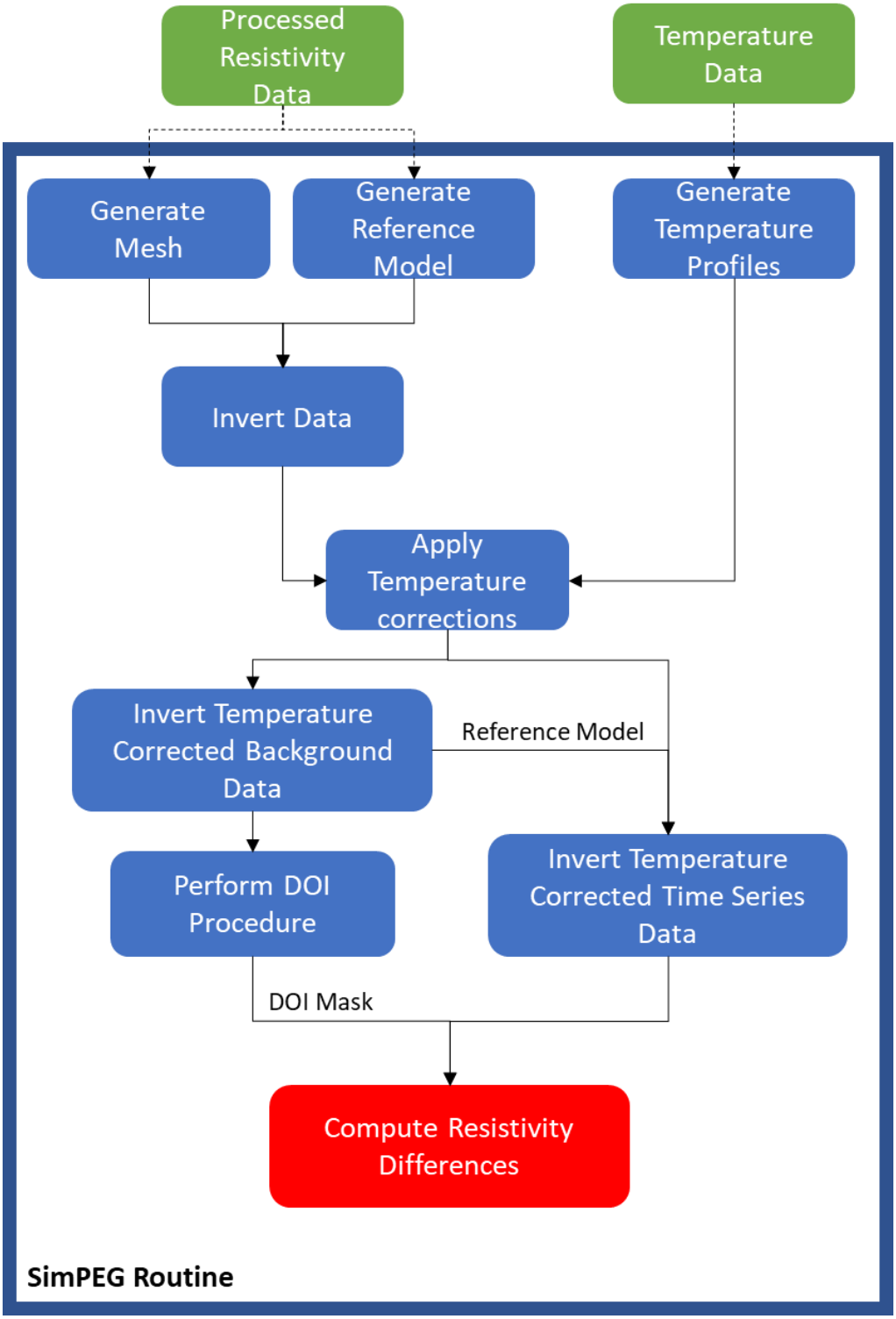
Processed Resistivity Data
Temperature Data
Generate Mesh
Generate Reference Model
Generate Temperature Profiles
Invert Data
Apply Temperature corrections
Invert Temperature Corrected Background Data
Reference Model
Perform DOI Procedure
Invert Temperature Corrected Time Series Data
DOI Mask
Compute Resistivity Differences
SimPEG Routine

Fig. 4.1. Work flow of SimPEG inversion routine. Green boxes are data inputs, blue boxes are procedures performed inside SimPEG's framework, and the red box is the output data.

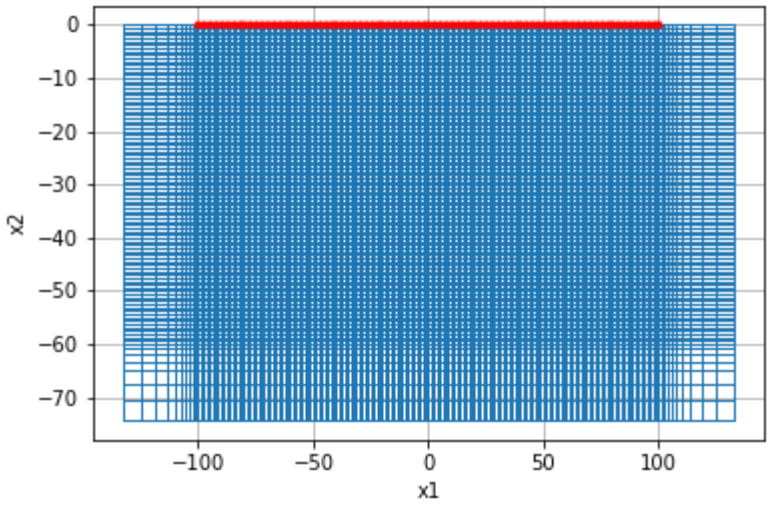

Fig. 4.2. Mesh design for Line 1 2.5m and Line 3 2.5 m. The mesh contains 18540 cells. The core cells are 1.25 x 0.62 m. 7 padding cells were added on the left, right and bottom of the mesh using an expansion factor of 1.3. The electrode positions are shown in red.

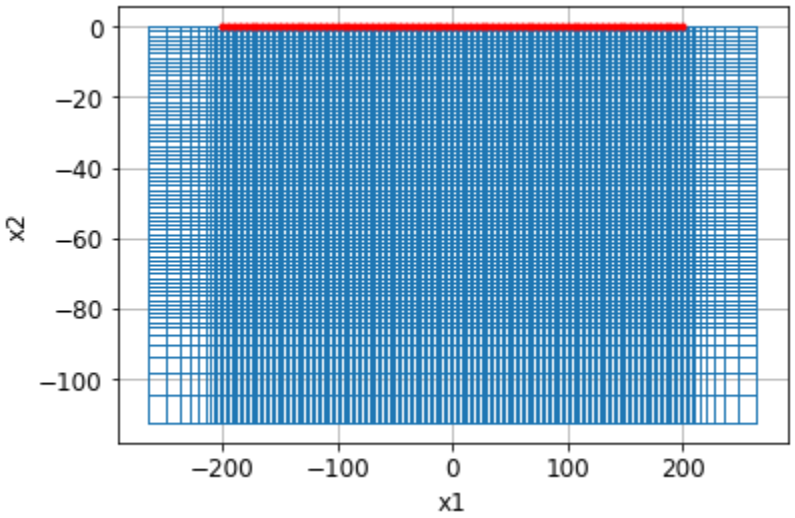

Fig. 4.3. Mesh design for Line 1 5m. The mesh contains 13320 cells. The core cells are 2.5 x 1.25 m. 7 padding cells were added on the left, right and bottom of the mesh using an expansion factor of 1.3. The electrode positions are shown in red.

4.2.3.2 Reference Model and Parameter Selection

The reference model used for the initial inversion of the background data is a homogeneous half space with a single value of resistivity. A histogram of the apparent resistivities in the data set aids the choice of initial resistivity value by picking a resistivity value that represents the median value of the data. Employing this approach, a value of 55 Ωm was chosen for the initial value of all three survey Lines.

The choice of regularization parameters discussed in the previous section was an iterative process. A large batch of inversions on the background data set were performed, each with a different combination of α parameters and uncertainty parameters. An initial $floor$ value was chosen by looking at a histogram of the voltage data and estimating the standard deviation in the smallest valued measurements (Figure 4.4). Accordingly, the uncertainty in those values was estimated at 0.001 Volts and an initial value for $\%|d_i|$ was chosen at 5%. The value of $\%|d_i|$ can be varied depending on the confidence in the data, a very small value will tend to overfit the data, whereas too large a value will fail to resolve resistivity structure. Different combinations of regularization parameters were trialed to create resistivity models for the three lines that replicated the resistivity structure interpreted from the core logs. The models were assessed on their likeness to the core logs and whether the resistivity structure fit the expected geological structure. The fluvial environment in which the fine-grained sand was deposited likely resembled braided stream architecture. The groundwater flow direction in the region runs NW to SE or parallel to Line 1. This might suggest that the channels deposited in the quaternary run parallel to this azimuth. The relatively laterally continuous high resistivity structures in Figure 4.5 support this hypothesis. Likewise, the increased level of lateral heterogeneity in the orthogonal Line 3

(Figure 4.7) suggests that this line cuts the channel structures perpendicular to their flow direction. Smoothing was required as the depositional history of the sediment would mean some gradual changing of grain size as opposed to very sharp contrasts in minerology that would be created by bedrock with extremely large resistivity. Final values for the background inversion parameters are shown in table 4.1.

ERT LINE	α_s	α_x	α_z	$floor$	$\%\|d_i\|$	β	RMS	ITERATIONS
LINE 1 2.5 M	1	50	50	0.001	0.5	10	0.4%	20
LINE 1 5 M	1	10	10	0.001	0.5	10	0.3%	17
LINE 3 2.5 M	1	50	50	0.001	0.5	10	0.4%	20

Table 4.1. Inversion parameters for the background inversions of each line.

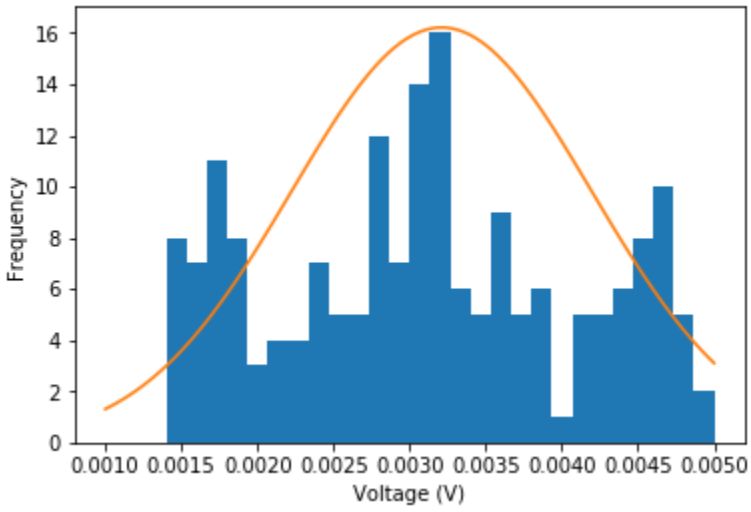

Fig 4.4 Histogram of voltage measurements showing an approximate Gaussian distribution about the smallest measured values. The Gaussian distribution has a mean of 0.0032 V and a standard deviation of 0.001 V. A value for the error floor of 0.001 V was chosen based on this histogram

4.3. Temperature Correction

As discussed in Chapter 2, electrical resistivity measurements are a function of the bulk resistivity of the volume under investigation. To isolate the resistivity changes resulting from the presence of methane gas, the changes due to temperature fluctuations during the injection must be accounted for. For a detailed description of the temperature correction procedure, readers are referred to Hayley et al. (2010), and an outline of the methodology as pertains to the inversion routine is covered below.

The raw data recorded in the field, $\boldsymbol{d}_{obs}$, are first inverted using the inversion routine with a β cooling schedule to output a resistivity model, $\boldsymbol{m}_{est}$, with the corresponding model response $\boldsymbol{d}_{est}$. For the β cooling schedule SimPEG chooses a value of β from the largest eigenvalue of the sensitivity matrix. This value is kept for two iterations and then divided by 5 for the next iteration. This procedure is repeated until the stopping criteria is met. For the beta cooling schedule the regularization parameters are $\alpha_{\boldsymbol{s}} = 10$, $\alpha_{\boldsymbol{x}} = 1$, $\alpha_{\boldsymbol{z}} = 1$. The model is then corrected to a temperature equivalent model using the procedure from Hayley et al. (2007), whereby, the resistivity values of the model estimate, $\boldsymbol{m}_{est}$, are converted to conductivity values as $\sigma = \frac{1}{\rho}$ and the following equation is applied:

$$\sigma_{std} = \left[\frac{m(T_{std}-25)+1}{m(T_i-25)+1}\right]\sigma_i, \tag{4.25}$$

where σ_{std} is the electrical conductivity at the standardized temperature, T_{std}, T_i is the in-situ temperature estimated from field data, σ_i is the in-situ conductivity taken from $\boldsymbol{m}_{est}$, and m is an empirically derived constant, which for our experiment is 0.02 $°C^{-1}$, and the standardized temperature was set to 6 $°C$. The result is a standard temperature equivalent model $\boldsymbol{m}_{est} + \Delta\boldsymbol{m}$,

where $\Delta \boldsymbol{m}$ is the model temperature correction, that has an associated model response $\boldsymbol{d}_{est}^{TC}$. $\boldsymbol{d}_{est}^{TC}$ is calculated by forward modelling the newly temperature corrected model, and the observed data are then temperature corrected by:

$$\boldsymbol{d}_{obs}^{TC} = \boldsymbol{d}_{obs} + (\boldsymbol{d}_{est}^{TC} - \boldsymbol{d}_{est}). \tag{4.26}$$

The temperature corrected background data sets are then inverted using the parameters in Table 4.1 and subsequently used as the reference models for the temperature corrected time-lapse inversions (Figure 4.1).

4.4. Time-Lapse Inversions

The methodology of time lapse inversion has been the subject of many research papers in the past 20 years (e.g. Daily et al., 1992, Labreque and Yang, 2001, and Miller et al, 2008). This study utilizes the routine outlined in Miller et al. (2008) and is referred to in the literature as cascaded time-lapse inversion. This approach uses the inverted model of the background data set as the reference model for subsequent time series inversions (Figure 4.1). Within the SimPEG routine the model regularization term is given more weight than for the background inversion to minimize the difference between the temperature corrected background model and the inversion of subsequent temperature corrected time steps. Hayley et al. (2011) note that artifacts in the initial inversion will proliferate through the subsequent inversions and will need to be smoothed. Consequently, care was taken on the initial inversion to attain a geologically plausible model with minimal artifacts. The necessity of temperature corrections led to the use of the SimPEG framework in which we can comfortably apply the cascaded time-lapse inversion scheme. There

are more sophisticated time lapse inversion methods outlined in Haley et al. (2011), however, due to its simplicity and the scope of this project the aforementioned technique was chosen.

4.5. Depth of Investigation Evaluation

In the resulting inversion, there are areas of the model that are insensitive to the data. Accordingly, an estimate of the reliability of the model with depth prevents over-interpretation of the model. The appraisal of the sensitivity to the data in this study is performed by evaluating the data error-weighted cumulative sensitivity (Nguyen et al., 2009 and Kenma et al., 2002):

$$s = \sum_{i=1}^{N} \left[\frac{(J)_{ij}}{\varepsilon_i}\right]^2 = diagonal(\boldsymbol{J}^T \boldsymbol{W}_d^T \boldsymbol{W}_d \boldsymbol{J}). \quad (4.27)$$

Here N is the number of model parameters and s is an array of cumulative sensitivity values for each cell in the model. This creates a map describing how the model space is 'covered' by the data (Kenma et al, 2002). The choice of cutoff value for the cumulative sensitivity is somewhat arbitrary. Hence, the choice of cutoff value, 0.2, was chosen based on the agreement of the structure from the core logs and the resistivity structure of the inversions. The application of the sensitivity mask is shown in figures 4.5, 4.6 and 4.7 and its position in the procedure in indicated in Figure 4.1.

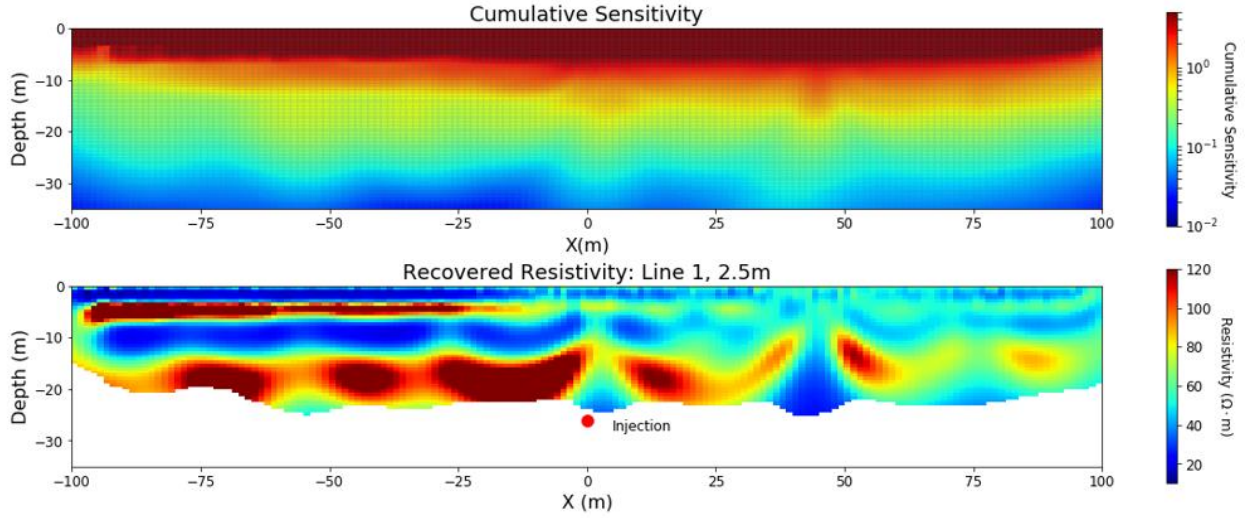

Fig. 4.5. Plot of cumulative sensitivity for Line 1 2.5 m (Top) applied with a 0.2 cutoff to the background model (Bottom).

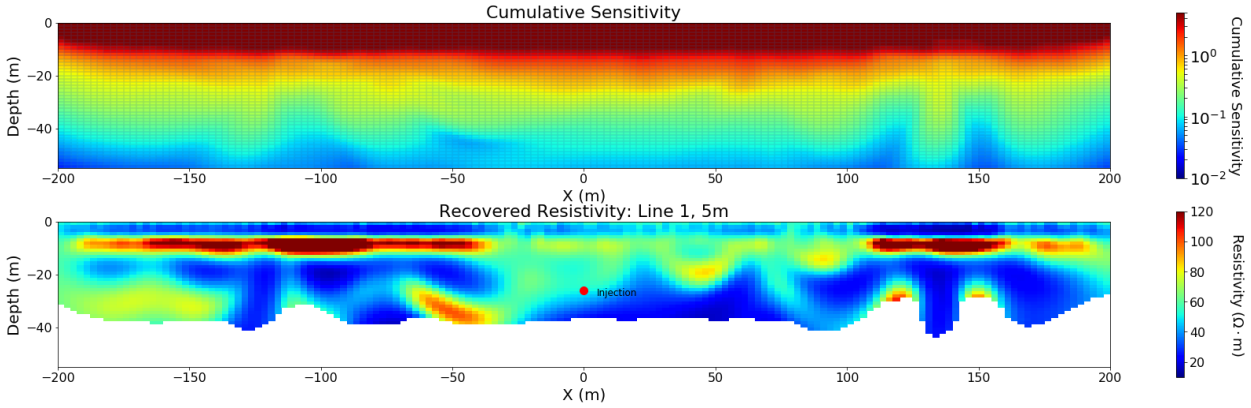

Fig. 4.6. Plot of cumulative sensitivity for Line 1 5 m (Top) applied with a 0.2 cutoff to the background model (Bottom).

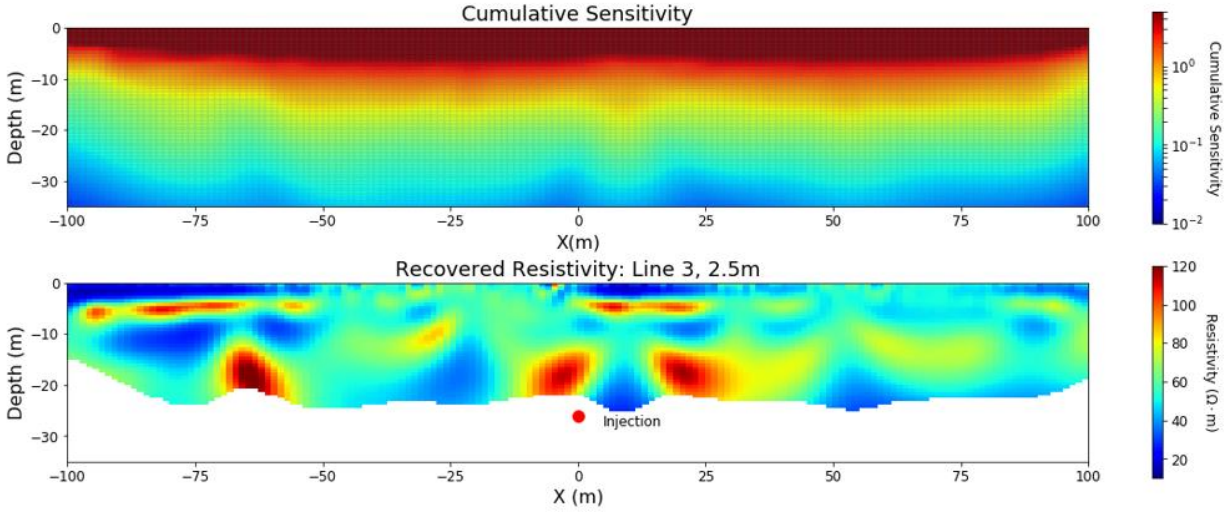

Fig. 4.7. Plot of cumulative sensitivity for Line 3 2.5 m (Top) applied with a 0.2 cutoff to the background model (Bottom).

CHAPTER 5: RESULTS

Results

This chapter presents and discusses the results of the time-lapse inversions for the three lines: Line 1 2.5m, Line 1 5m, and Line 3 2.5m. We will look at the background inversions, i.e. pre-injection, and the temperature corrections before finishing with the cascaded time-lapse inversion differences.

5.1 Temperature Data

The recorded subsurface temperature profiles for each of the surveys are shown in Figure 5.1. Each graph shown is an average from the temperature profiles recorded in boreholes MW9, MW11, and MW12. Unfortunately, the data obtained from MW10 were not useful due to transmission losses in that loop and were therefore not included. The DTS interrogator was active from June 6th through to August 13th. Therefore, the temperature profile of June 6th was used as a proxy for June 5th and the temperature profile of August 13th was used as a proxy for the September 8th and 9th data sets.

5.2 Background Inversions

The resistivity data were inverted by iterating different combinations of the regularization parameters until the resistivity model produced had a similar structure to that of the core logs. The uncertainty parameters were relaxed so that the inversion would perform enough iterations to “overfit” the data. Miller et al. (2008) recommend this procedure to resolve the total

background structure before the time-lapse inversions, ensuring as much as possible that changes in the time-lapse inversions are due to the data and not further refinement of the background resistivity structure. The data were then temperature corrected to a standard temperature of 6 degrees Celsius using an m value of 0.02 via the method of Hayley et al. (2010), outlined in Chapter 4. The temperature corrected resistivity data were then inverted using the relaxed uncertainty parameters (Table 4.1) until subsequent iterations varied <5% around the injection zone.

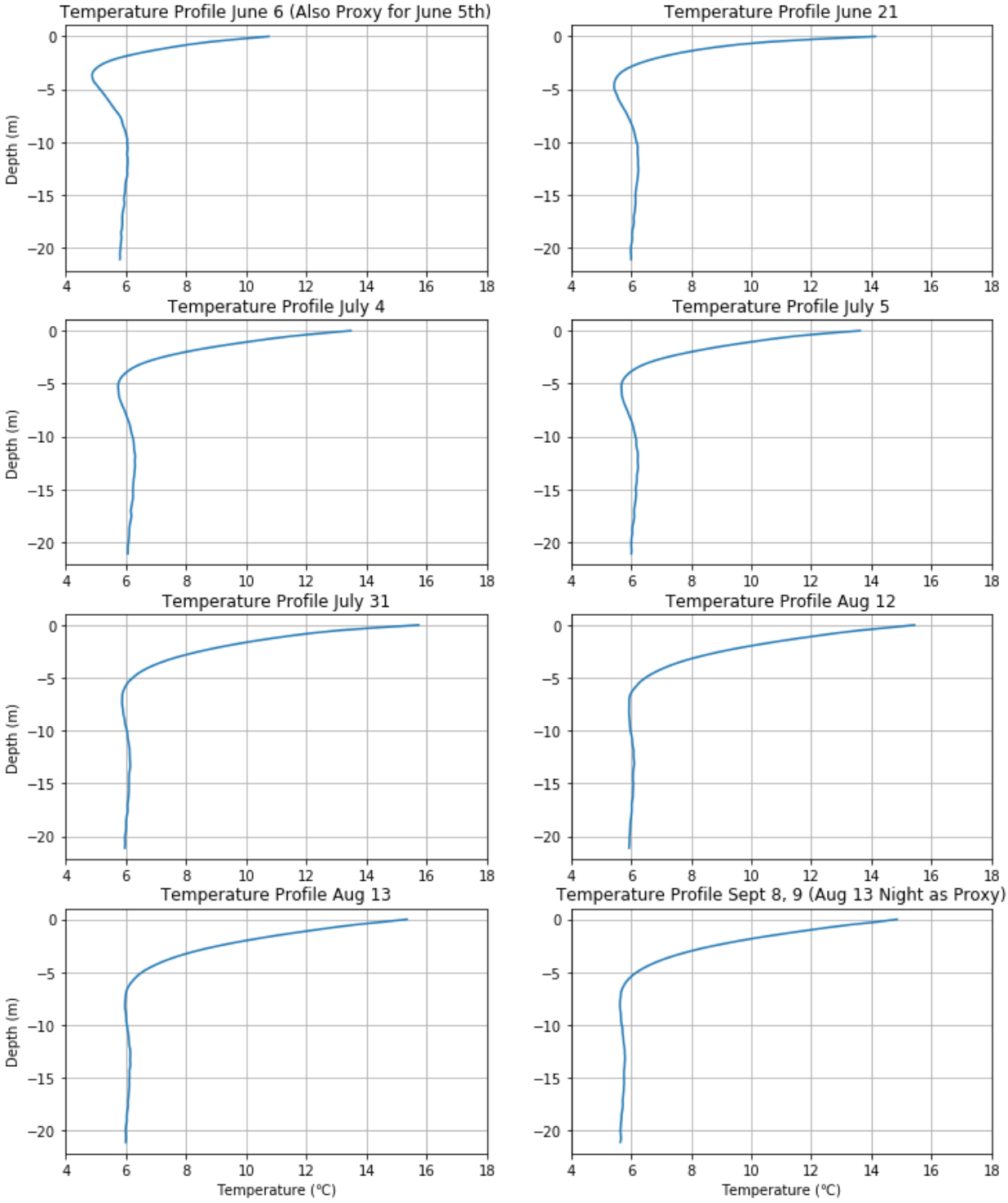

Fig. 5.1. Temperature profiles from distributed temperature sensors used for temperature corrections. The curves are an average of the temperature profiles from MW9, MW11, and MW12. The profile of MW10 was not used due to transmission losses.

5.2.1 Line 1 2.5 m

We begin by looking at the inversion of Line 1 2.5m. The data for the background survey on June 5th contains 2947 measurements and required no editing, or removal of data points prior to inversion. The temperature during data collection was approximately 12 ℃ with light rain. The resistivity data were inverted using regularisation parameters of $\alpha_s = 1, \alpha_x = 1, \alpha_z = 1$, and $\beta = 10$. A homogeneous half space of 55 Ωm was used as the reference model for the inversion based on the median value of apparent resistivities shown in the histogram in Figure 5.2. The inversion took 20 iterations and the resistivity differences between the non-corrected and temperature corrected data are shown in Figure 5.3. The resistivity model shows a high resistivity layer (60-150 Ωm) from approximately 14 to 25 m bgs that is between two low resistivity layers (10-30 Ωm). The high resistivity layer is attributed to the fine-grained sand seen in the core logs and corresponds to our aquifer interval. Similarly, the two low resistivity layers correspond to a higher clay content and the upper clay layer acts as an aquitard to the confined aquifer below. The injection location at 26 m bgs is shown in figure 5.3 and appears to have targeted the base of the aquifer successfully.

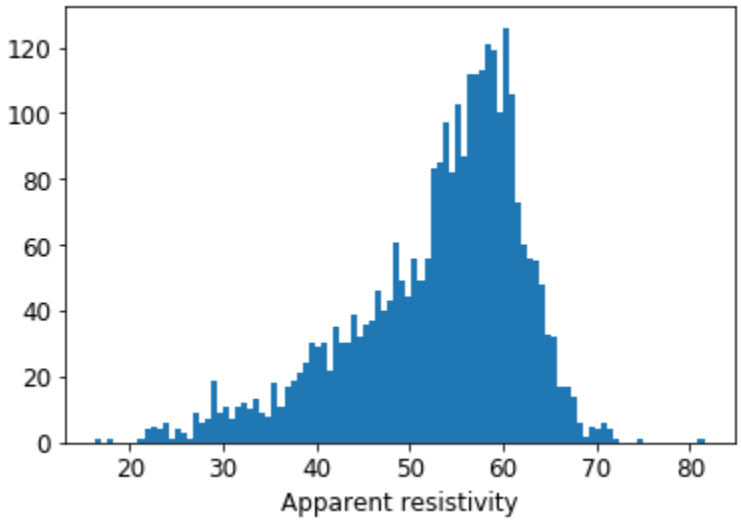

Fig. 5.2. Histogram of apparent resistivity measurements from the background survey of Line 1 2.5 m. The distribution provides a guide for a choice of reference model. 55 Ωm was chosen based on the median of the data.

5.2.2 Line 1 5 m

The data for the background survey contain 2767 measurements, which were recorded on June 6th and required editing for erroneous data points. The conditions of the survey were damp in the near surface due to rain the previous day and the temperature was approximately 12 $°C$. The resistivity data were inverted using regularization parameters of $\alpha_s = 1, \alpha_x = 10, \alpha_z = 10,$ and $\beta = 10$. A homogeneous half space of 55 Ωm was used as the reference model for the inversion based on the histogram of the apparent resistivities shown in Figure 5.4. The temperature corrected inversion took 17 iterations and the resistivity differences between the non-corrected and temperature corrected data are shown in Figure 5.5.

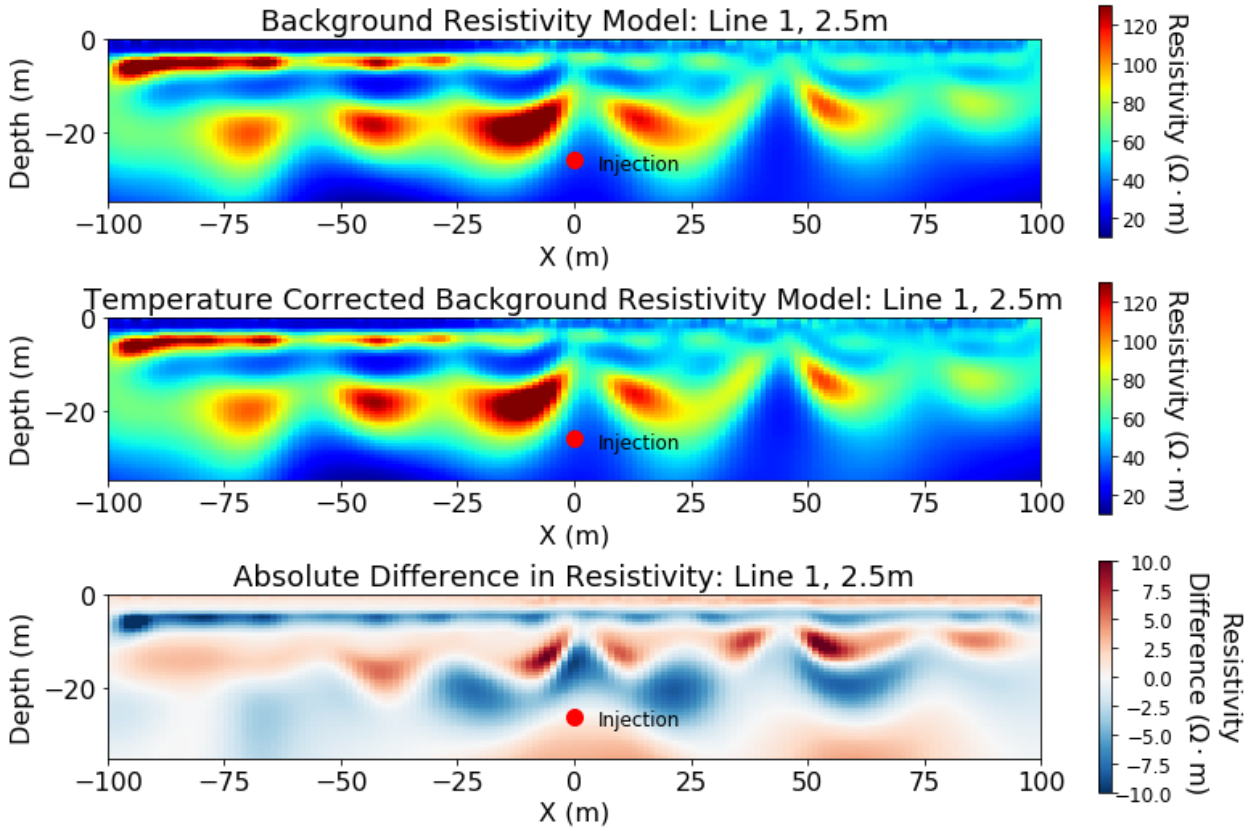

Fig. 5.3. Plots of the background resistivity inversions for non-corrected (Top) and temperature corrected data (Middle). The bottom image shows the absolute difference in resistivity between the two models (Bottom). The model matches the core logs in a first order sense, that is, a high resistivity layer sandwiched between two low resistivity layers. The high resistivity layer is the fine-grained sand aquifer and the low resistivity layers are clay and silt.

The resistivity model shows an area of higher resistivities, 60-120 Ωm, from approximately 10 to 26 m depth bgs around the injection zone that becomes shallow and thin with distance away from the injection site. This layer is interpreted to be our aquifer interval. Above and below the aquifer interval the model is dominated by low resistivities between 10-30 Ωm. As noted previously, the high resistivities are attributed to coarser sediment such as the fine-grained sand seen in the core logs. The low resistivity areas correspond to a high clay

content and the laterally continuous upper clay layer acts to confine the aquifer below. The resistivity models of Line 1 2.5 m and Line 1 5 m are inline and show a nominally good agreement with the interpreted resistivity structure at the site. The 2.5 m spacing line provides higher resolution in the injection region and near surface, whereas the 5 m Line 1 provides greater depth of investigation.

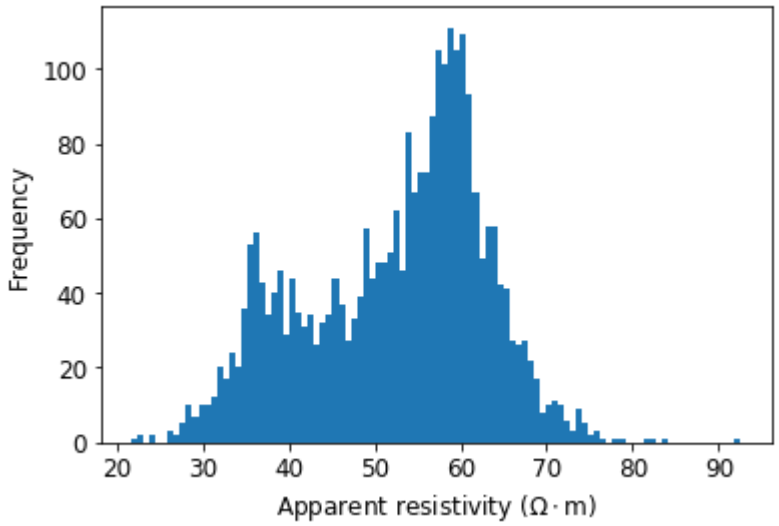

Fig 5.4. Histogram of apparent resistivity measurements from the background survey of Line 1 5 m. The distribution provides a guide for a choice of reference model. 55 Ωm was chosen.

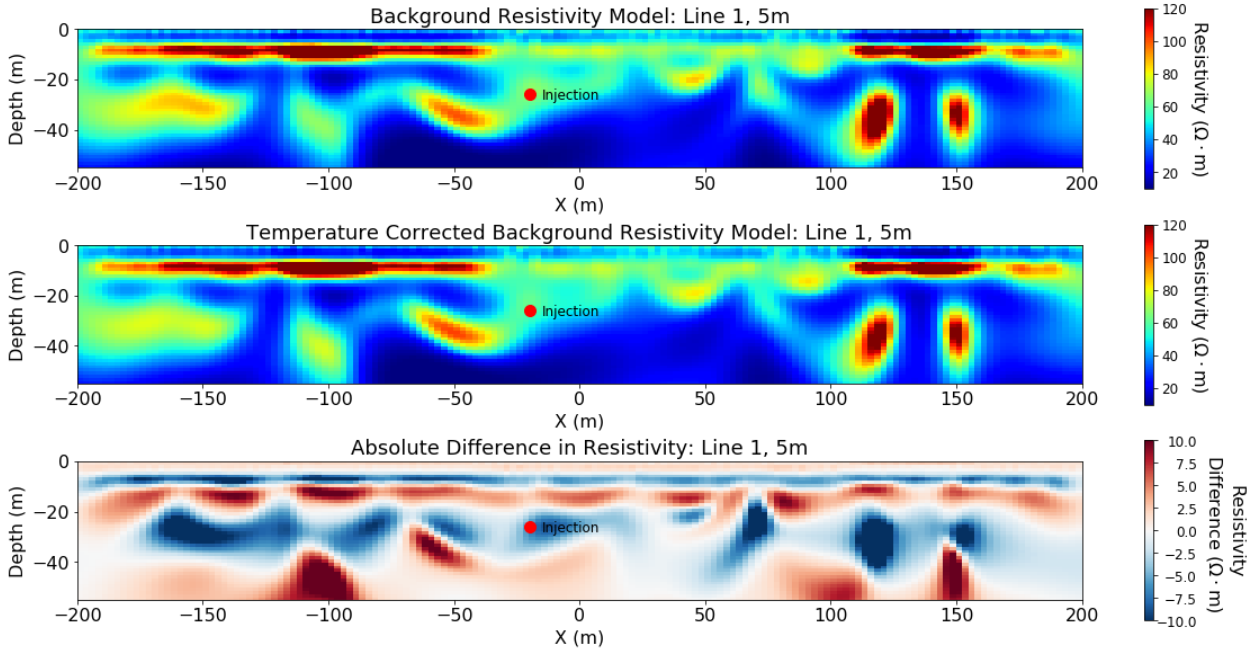

Fig. 5.5. Plots of the background resistivity inversions for non-corrected (Top) and temperature corrected data (Middle). The bottom image shows the absolute difference in resistivity for the two models (Bottom).

5.2.3 Line 3 2.5 m

The data for the background survey of Line 3 were collected on June 5th and contain 2944 measurements. The data were of good quality and did not require editing. The conditions during data collection were wet and the temperature was approximately 12 $°C$. The resistivity data were inverted using regularization parameters of $\alpha_s = 1, \alpha_x = 50, \alpha_z = 50$, and $\beta = 10$. A homogeneous half space of 55 Ωm was used as the reference model for the inversion based on the histogram of the apparent resistivities shown in Figure 5.6. The temperature corrected inversion took 20 iterations and the resistivity differences between the non-corrected and temperature corrected data are shown in Figure 5.7.

The resistivity structures in Line 3 are not as laterally continuous as Line 1 2.5 m. Within the upper 10 m there are small pockets of thin high resistivity layers (~100 Ωm). A layer of low resistivity material (10-30 Ωm) lies above the majority of the high resistivity zone between 10-15 m depth and is interpreted to be a confining layer for the aquifer zone which lies below. The aquifer interval comprises of higher resistivities, between 60-120 Ωm, and is laterally discontinuous. Low resistivity material (10-30 Ωm) that underlies the aquifer zone readily intrudes up to depths of 15-20 m. Once more, the general structure of the subsurface is that of higher resistivity material capped above and below by low resistivity clay rich sediment. The resistivity model agrees with the Line 1 2.5 and 5 m models in a general sense, however, the Line 3 model presents more evidence of lateral heterogeneity.

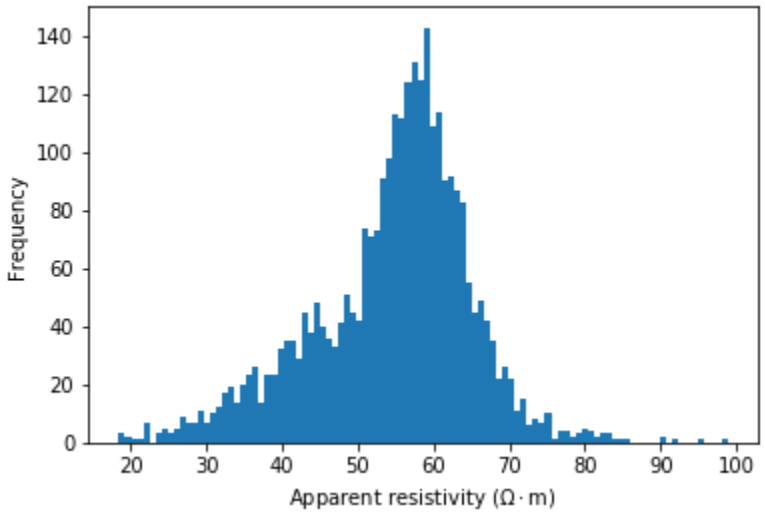

Fig 5.6. Histogram of apparent resistivity measurements from the background survey of Line 3 2.5 m. The distribution provides a guide for a choice of reference model. 55 Ωm was chosen.

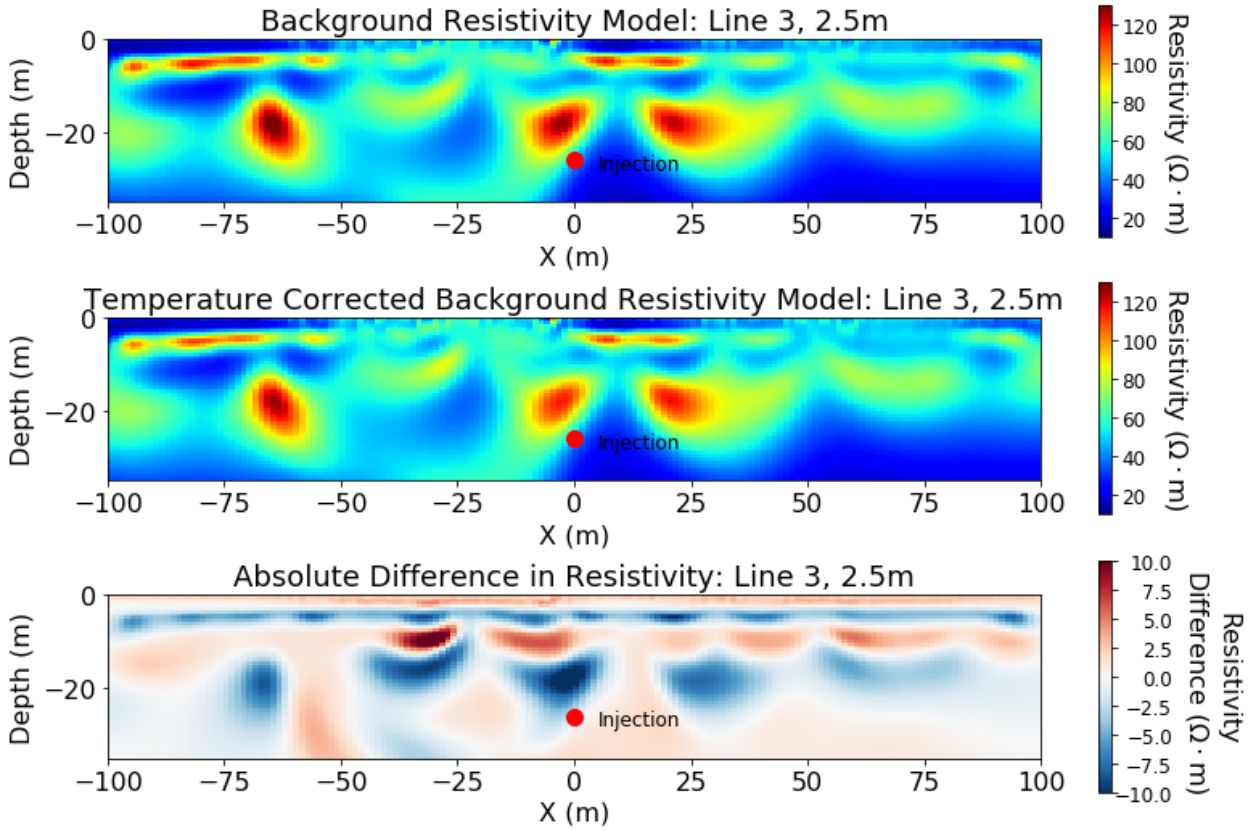

Fig. 5.7. Plots of the background resistivity inversions for Line 3 2.5 m. The non-corrected model is shown in the top image (Top), temperature corrected model in the middle image (Middle), and the bottom image shows the absolute difference in resistivity for the two models (Bottom).

5.3 Time-Lapse Inversions

For each of the time-lapse inversions, the temperature corrected background survey models were used as the reference models for all the subsequent times. The reference model regularization term, α_s, was increased to penalise deviation from the background model. The reason for this is that we are confident in the resistivity structure and the aim is to isolate changes in resistivity due to data via the presence of gas, not resolve more background structure (Miller et al., 2008).

Given the RMS errors for the time-lapse inversions are < 3 %, changes in resistivity less than 3% are not considered to be significant enough to be due to the presence of free phase gas.

5.3.1 Line 1 2.5 m

After processing the time series data for Line 1 2.5 m, the data for days 9, 23, 49, 61, and 88 contained 2756, 2947, 2753, 2735, and 2724 measurements respectively. There were issues with a take-out on one of the cables during acquisition of the data sets on days 61 and 88 which produced erroneous measurements. Consequently, some artifacts of the bad data remain in the upper SE portion of the difference images for these two models. The weather for the surveys after the injection began was between 20-30 ℃ and dry other than for day 88 which was ~12℃ and raining. During the time-lapse inversions the model regularization term was increased to $\alpha_s = 20$, adding weight to the reference model, and the smoothing parameters were set to $\alpha_x = 1$ and $\alpha_y = 1$. The inversions converged in one iteration with RMS errors of 1.1%, 0.7%, 1.4%, 1.3%, and 2.2% for days 9, 23, 49, 61, and 88 respectively. The percentage differences between the background data and the different time series data are shown in Figure 5.8.

Measurements on day 9 of the injection show increases in resistivity of up to 7% 10-25 m downgradient (SE) of the injection point starting at approximately the injection depth with vertical extent up to 10 m bgs. At 10 m bgs, resistivity increases of 5-17% are seen upgradient (NW) of the injection location. The most significant increases in resistivity (17%) are seen 50 m upgradient of the injection point at 10 m depth. The changes seen on day 23 mirror that of day 9, the most notable change is a reduction in the anomaly 50 m upgradient from a 17% to a 7% increase. This anomaly has also grown in lateral extent from the injection location to 85 m

upgradient. By day 49 the observed changes between 8 -12 m depth have increased in magnitude across the profile by approximately 5% (Figure 5.11). The image shows laterally continuous increases between 5-15% at approximately 10 m depth across the whole profile. Day 61 shows a similar profile to day 49, however, the magnitude of changes have decreased by 2% in the 8-12 m depth zone (Figure 5.11) and the increases are less connected. This might be explained by some gas escaping through the monitoring port of MW2 during water testing (Tim Cary field observation). If significant amounts of gas did escape to surface during this time, the saturation of gas around the monitoring port could have declined commensurately. The resistivity changes of day 88 (post-injection) between 8-16 m depth are smaller in magnitude to days 49 and 61 (Figure 5.11). The laterally continuous increases seen in previous images are more sporadic on day 88. Around the injection zone and upgradient the resistivity increases have returned to background levels. There still remains a localized increase of 15-17% 45 m SE of the injection at 10 m bgs.

5.3.2 Line 1 5 m

After processing the time series data for Line 1 5 m, the data from days 9, 23, 49, 61, and 88 contained 2746, 2769, 2745, 2732, and 2661 measurements respectively. There were issues with a take-out on one of the cables during acquisition of the data sets on days 49, 61 and in particular day 88. Some artifacts of the erroneous data remain in the upper NW corner of the differences image for day 49 and the upper SE portion of the differences image for day 61. The differences image for day 88 show significant artifacts to the SE of the injection due to poor data quality. The weather for these surveys was mostly hot and dry other than for day 88 which was

12 ℃ and raining. During the time-lapse inversions the model regularisation term was increased to $\alpha_s = 20$ and the smoothing terms were set to $\alpha_x = 1$ and $\alpha_y = 1$. The inversions converged in one iteration other than day 88 which took 3 iterations. The RMS errors for days 9, 23, 49, 61, and 88 were 0.4%, 0.3%, 0.7%, 0.4%, and 1.4% respectively. The percentage differences between the background model and the different time series' models are shown in Figure 5.9.

The difference image for day 9 shows a small area of increases in resistivity between 3-5% 20 m downgradient of injection between 10-20 m bgs. Additionally, 50 – 130 m upgradient of the injection, resistivity increases of 5-13% are seen between 10-26 m bgs. Lastly, there are some small changes of 3-5% resistivity increase observed from 120-170 m downgradient of the injection. On day 23 the changes around the injection zone have increased in magnitude. This is illustrated by increases of 3-6% 10-70 m downgradient of injection and increases of 3-10% extending 150 m upgradient from the injection. Finally, increases of up to 13% are seen downgradient at 150m. Moving to Day 49, the average resistivity in the depth interval of 12-16 m increased by 3% (Figure 5.11). Increases in resistivity between 6-10% are laterally continuous from 70 m downgradient to 150 m upgradient of the injection. The area of increased resistivity centered 160 m downgradient of injection remains but has decreased to 10%. Day 61 also shows the extensive lateral increases in resistivity seen on day 49, however, the average magnitude of the increases has reduced by 2% (Figure 5.11). Finally, the downgradient side of the day 88 image shows a lot of variability that is likely due to artifacts in the inversion resulting from the quality of the data. Nevertheless, we see an area of approximately >20% resistivity increase 40 m downgradient of injection and at 120 m downgradient of injection. Increases in resistivity still remain between 3-8% 50-130 m upgradient. Finally, the resistivity increases around the injection location of the previous days are no longer observed.

5.3.3 Line 3 2.5 m

The time series data for Line 3 2.5 m from days 9, 22, 49, 62, and 89 contained 2759, 2768, 2732, 2734, and 2716 measurements respectively after data processing. There were issues with a take-out on one of the cables during acquisition of the data sets on days 49, 62 and 89. There are some artifacts of the erroneous measurements seen near the surface at 85 m in the difference images of these data sets. The weather for these surveys was mostly hot and dry other than for day 89 which was 12 ℃ and raining. For the time-lapse inversions, the model regularization term was increased to $\alpha_s = 20$, and the smoothing terms were set to $\alpha_x = 1$ and $\alpha_y = 1$. The inversions converged in one iteration and the percentage differences between the background model and the different time series' models are shown in Figure 5.10. The RMS errors of the time-lapse inversions for days 9, 22, 49, 62, and 89 were 0.7%, 1.1%, 1.8%, 1.5% and 2.5% respectively.

The difference image from day 9 shows an increase in resistivity of 3-8% 10 m to the NE of the injection that extends upwards to a depth of 10 m. At 10m depth a small lobe of 3-4% increases extends 15 m to the NE. Additionally, there is a small pocket of 3-6% increase 25 m to the SW of center at 10 m depth and an area of up to 8% increase at 75 m SW of center and 10-15 m depth. Day 22 shows a similar pattern of changes to day 9. The area of resistivity increases 10 m to the NE of the injection remains, however, the attached side lobe has grown in lateral extent, reaching 40 m to the NE and the increases have grown to 8% within the lobe. The two areas of increased resistivity to the SW remain and have increased in magnitude by 2-5%. Additionally, a region of 3-6% resistivity increase has appeared 85 m to the NE of center. By day 49 the

centralized increases have grown further to 10% and now extend continuously across most of the profile between 7-20 m depth. This is highlighted by an approximately 4% increase in resistivity in the 8-12 m depth interval (Figure 5.11). The resistivity increases seen at 85 m NE of center have increased to 12% but are likely due to the cable errors during acquisition. Day 62 shows similar changes to day 49, however, there is a decrease of 2% in resistivity increases at the 8-12 m depth interval across the image (Figure 5.11). Of note, the SW side lobe of the central changes has greatly reduced, and only a small bulb of <5% increase remains extending to 10 m SW of center. The maximum change seen in the center of the image is now 8%, a drop of 2%. The large increases seen at 85 m to the NE of center have reduced to 6-8%. The image from day 89 shows a 7% reduction in resistivity increase in the 8-12 m depth interval across the profile (Figure 5.11). The areas of resistivity increases are now disconnected. The central region 10 m right of injection shows up to 12% increases, however the side lobes of this feature seen in previous images have disappeared. Finally, 60 m NE of injection, there is an area of 12% resistivity increases approximately 10 m bgs.

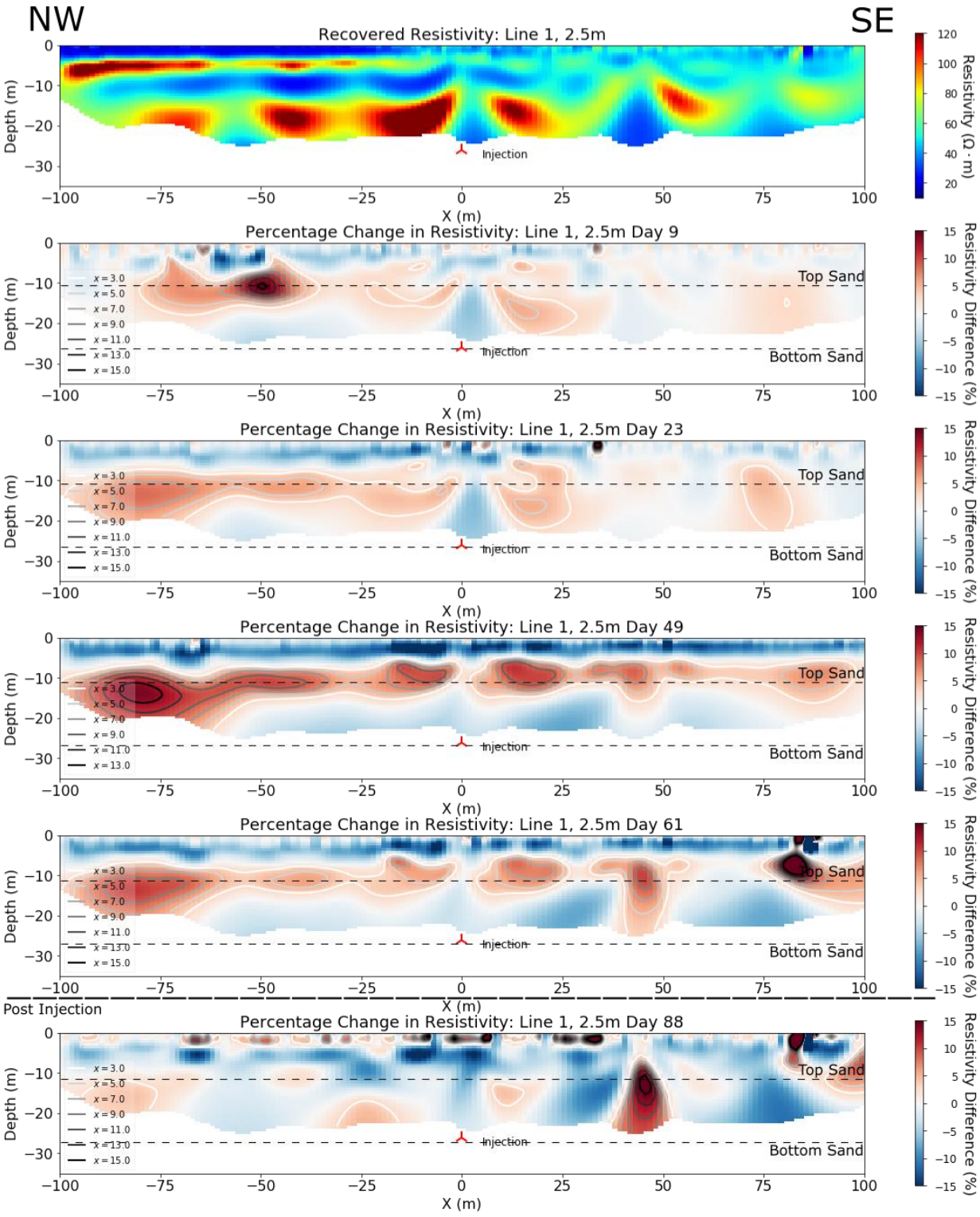

Fig 5.8. Percentage difference images for the time-lapse inversions of Line 1 2.5 m, with DOI mask applied. Images show the difference from the background inversion. Injection ceased on day 66.

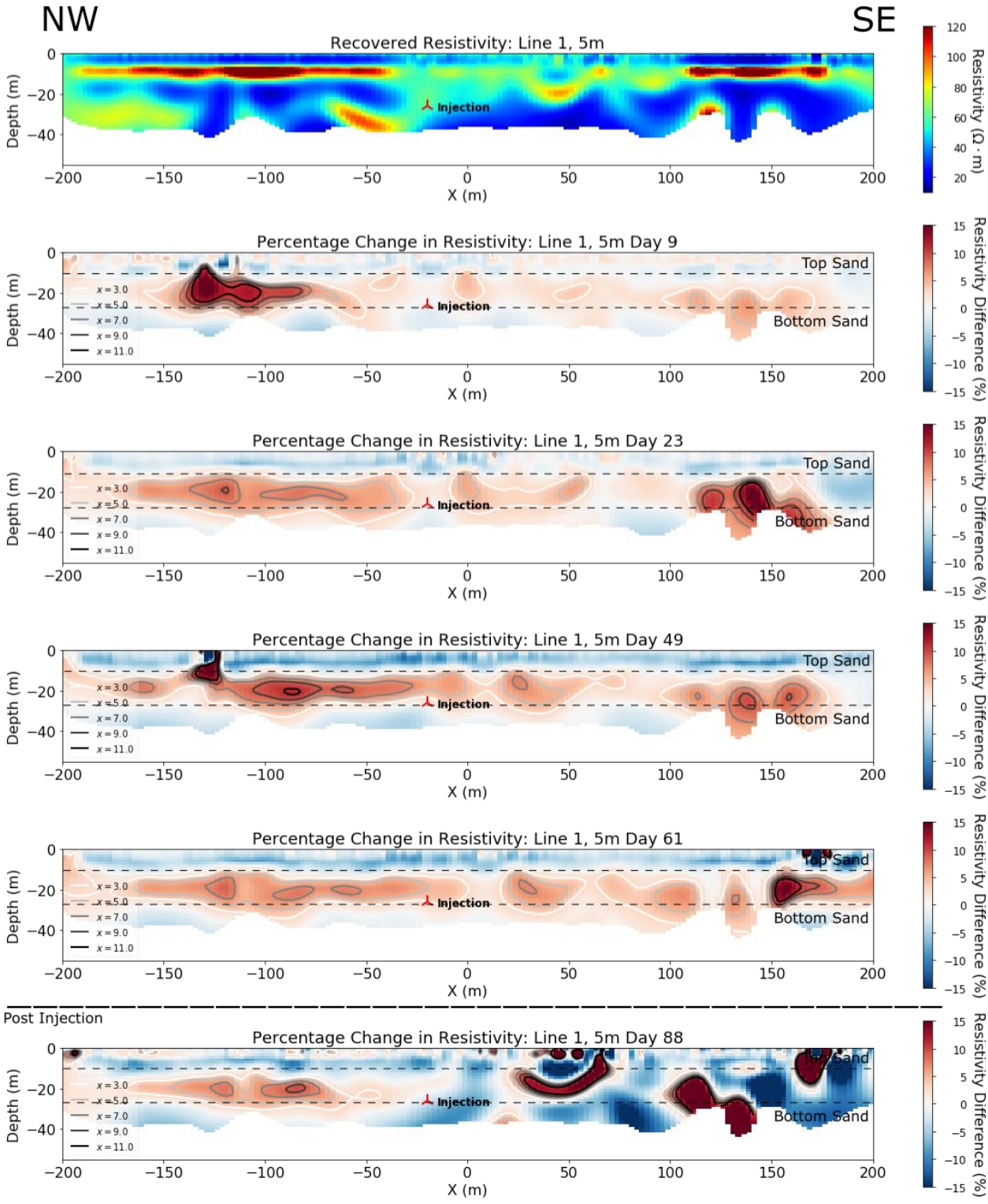

Fig 5.9. Percentage difference images for the time-lapse inversions of Line 1 5 m, with DOI mask applied. Images show the difference from the background inversion. Injection ceased on day 66.

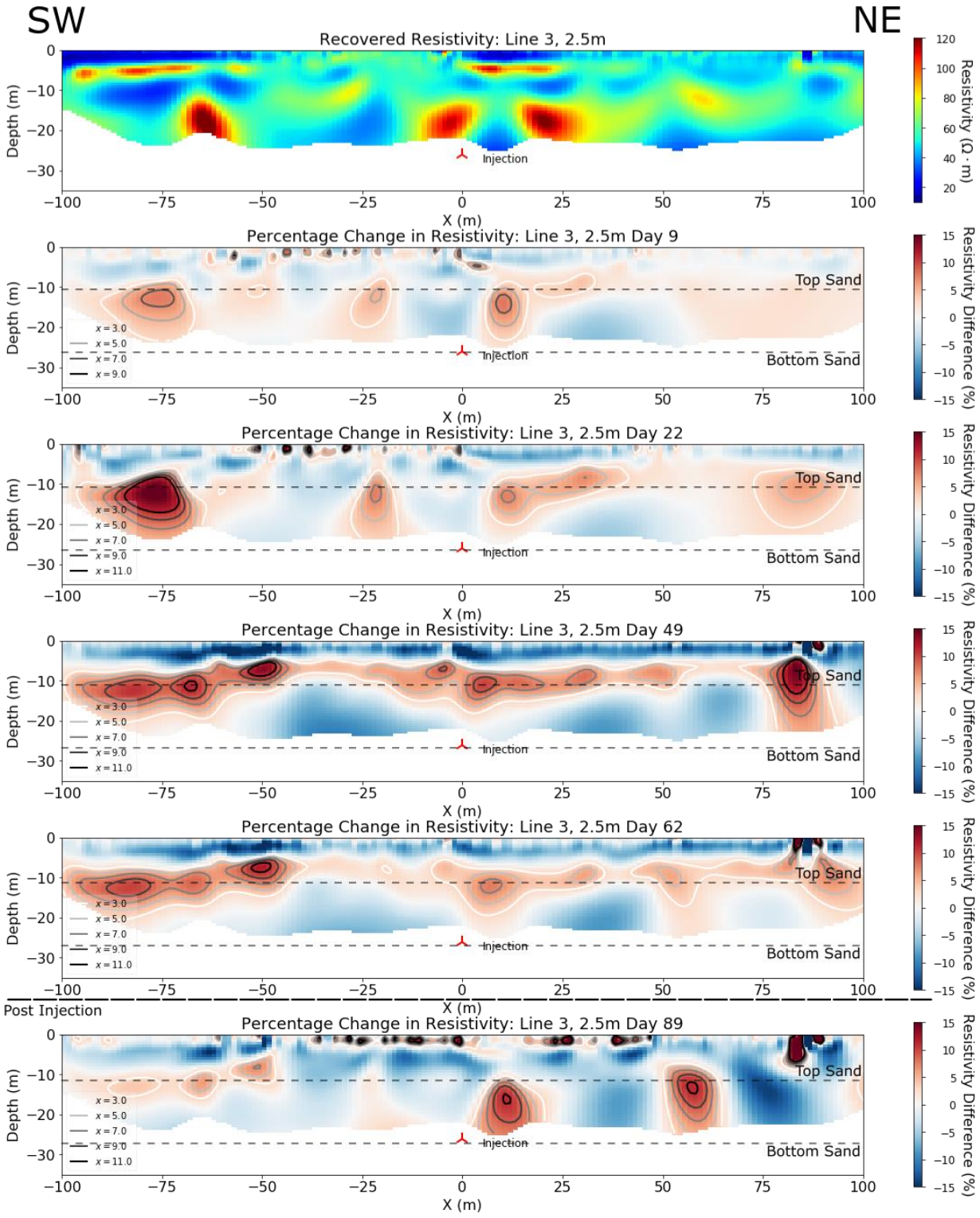

Fig 5.10. Percentage difference images for the time-lapse inversions of Line 3 2.5 m, with DOI mask applied. Images show the difference from the background inversion. Injection ceased on day 66.

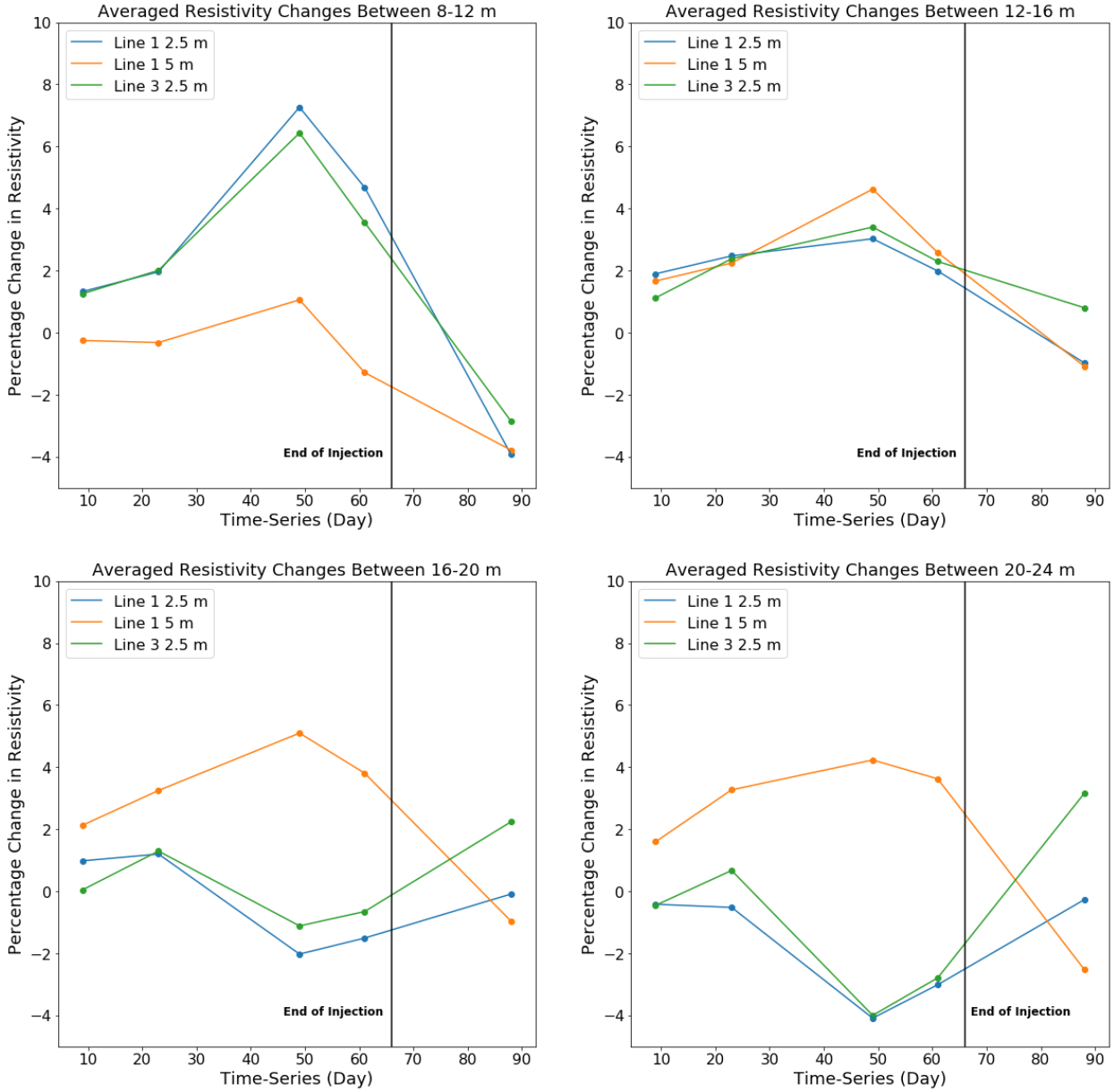

Fig. 5.11. Average percentage change in resistivity for four depth intervals: 8-12 m in the top left, 12-16 m in the top right, 16-20 m in the bottom left, and 20-24 m in the bottom right. The data show the largest increase in resistivity in the 8-12 m interval for Line 1 2.5 m and Line 3 2.5 m, suggesting pooling of gas beneath the clay aquitard that confines the aquifer at approximately 11 m depth.

CHAPTER 6: DISCUSSION AND CONCLUSIONS

6.1 Discussion

We can get an estimate of the expected changes in resistivity due to gas saturation by examining Archie's Law (Equation 2.7). Here we choose parameter values of a = 0.62, m = 2.15, and n = 2 for an unconsolidated sand (Asquith and Krygowski, 1982). An estimate for the pore fluid conductivity of 0.1 S/m is taken from the groundwater samples and the porosity of the aquifer sediment at the site was calculated in the lab to be 0.3 (Data courtesy of Jessie Chao). Figure 6.1 shows the percentage change in resistivity due to an increasing gas saturation. The curve shows that relatively little gas saturation is required for significant increases in resistivity. The time-lapse inversions show resistivity increases of around 15% at their strongest on day 49. A 15% increase in resistivity can be caused by approximately 7% gas saturation according to the curve in Figure 6.1. To get an estimate of whether there is enough gas in the ground to cause increases across the profile of 15% after 49 days we can perform an approximate calculation assuming a 0.5m layer of gas has pooled beneath the clay. The increases in resistivity near the edges of the profile appear to be centered on 75 m according to Figure 5.8. Therefore, we can assume a radial migration pattern of 75 m radius as an upper estimate. This is an upper estimate as there is likely extreme radial anisotropy in permeability due to the channelized nature of the deposited fluvial sands. The volume of this cylinder is 8836 m^3, assuming a porosity of 0.3 from the lab data this results in 2651 m^3 of pore volume. Therefore, to produce an increase in resistivity of 15% across the profile would approximately require 186 m^3 of injected gas. By the time of the day 49 survey there was ~74 m^3 of injected gas. This approximation shows that this

level of gas migration is possible. All of the assumptions made are upper bounds of what might be happening in the subsurface. Figure 5.8 shows that the increases across the profile can reach 15% but are generally lower and the porosity used is not the effective porosity of the sediment so likely results in a lower volume estimate. Based on the estimates of resistivity increase in Figure 6.1 and the fact that there are not any areas of resistivity increase >20 % in the time-lapse images, suggests that gas saturations within the aquifer remain at low levels < 10%. One possible explanation for this is that the propensity for the gas to migrate extensively laterally prevents the buildup of gas in a single location. There is also the possibility that the smoothing parameters of the inversion are reducing the magnitude of the increases and smearing them over a larger area in the model.

The results displayed in Chapter 5 highlight three key features that arise in all three time-lapse inversions. Firstly, there is a general trend of the resistivity increasing from day 9 through day 49. The increases in resistivity over time are interpreted to be due to the gradual increase in gas saturation as the total volume of injected gas increases, peaking at day 49. Figure 5.11 shows that there is a slight decrease in resistivity from day 49 to day 62 across all three profiles. There are a few possible mechanisms for this. Firstly, the gas may have continued to migrate beyond the aperture of the ERT arrays, this would mean that the gas saturations in the aquifer that we are capable of imaging would have reduced, resulting in lower resistivities. Secondly, due to the supposed migration of the methane gas, it is anticipated that the gas plume became thin and extensive as opposed to a thick bulb of gas. This presents a greater surface area for gas/groundwater interaction, creating more preferable conditions for mixing and dilution of free phase gas. This is supported by increased methane in solution observed in groundwater measurements by Jessie Chao at wells MW2, MW5 and MW12 around day 60.

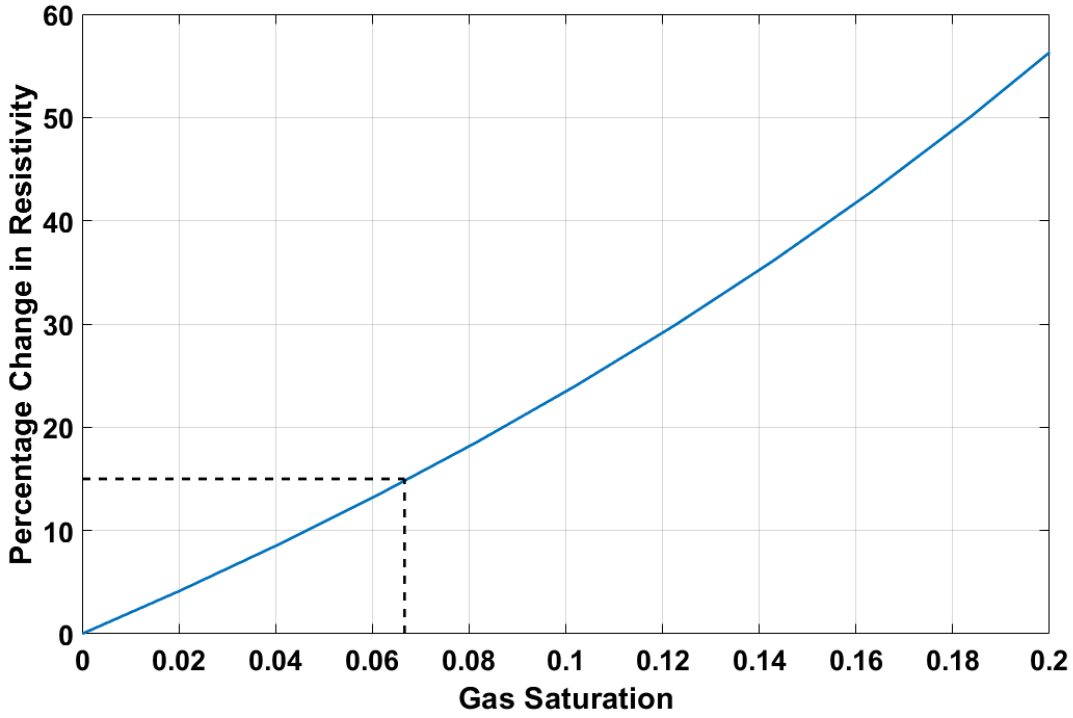

Fig 6.1 Percentage change in resistivity as a function of gas saturation based on Archie's Law. Parameter values are a = 0.62, m = 2.15, and n = 2 for an unconsolidated sand. Porosity at the site is 0.3 and pore fluid conductivity from water samples is 0.1 S/m. The dashed line shows that for ~7% increase in gas saturation there is a 15% increase in resistivity.

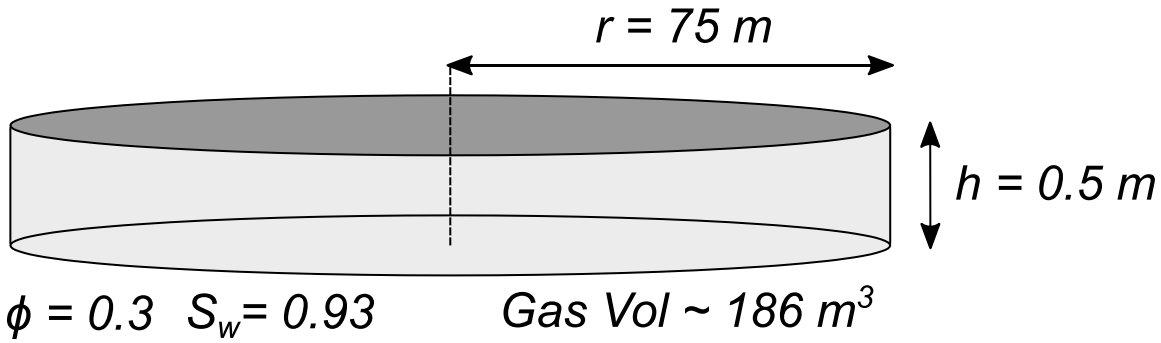

Fig 6.2 Schematic for the upper bound approximation for the required volume of gas to produce a 15 % increase in resistivity across the profile of Line 1 2.5 m. Approximation assumes a fluid conductivity of 0.1 S/m and a 7% gas saturation based on Figure 6.1.

The dissolution of methane gas would cause an increase in TDS, increasing the conductivity of the pore fluid. Furthermore, dissolution would remove free phase gas from the pore space, lowering gas saturations. Both of these effects would act to lower bulk resistivity. Thirdly, as mentioned in Chapter 2 there is the possibility of biodegradation of the methane. The effect of biodegradation would be twofold, not only would it mean less gas in the pore space but also an increase of TDS. The reduction of gas saturation would lower resistivity, as would the increase in TDS in the groundwater. However, Atekwana et al. (2004) suggest that the timescales for these types of biodegradation reactions are on the order of years and often the effects are seen at mature hydrocarbon spill sites. There is also the fact that biodegradation is favored by oxygen rich waters (Sauck, 2000), given our gas is interpreted to be trapped within a confined aquifer, the groundwater is likely low in oxygen, which would not favor biodegradation. Although this scenario could result in significant decreases in resistivity, of ~20 % (Sauck, 2000), it is the least likely explanation given the timing of 50-62 days after injection. The fourth scenario is that some of the gas migrated along a preferential pathway to surface and escaped the system. This scenario is most likely as there were field observations (Tim Cary) of methane gas escaping to surface around monitoring well MW2 on day 44 and 49. If a preferential pathway to surface was established any gas that was hydraulically connected to this pathway would likely escape to surface. The leakage event that was observed in the field around day 49 may have continued between day 49 and day 62, resulting in a decrease in resistivity that is observed in the time lapse images.

The second key feature is that on day 88 (or 89 for Line 3), which was 25 days post injection, the difference images show an overall reduction in resistivity increases. This suggests that as injection ceases, the processes mentioned above are no longer offset by the continued

injection of methane gas. It is probable that a combination of methane dissolution, escape to surface, continued migration outside the ERT arrays' aperture, and biodegradation cause a decline in gas saturation as well as an increase in pore fluid conductivity. This leads to buffered resistivity increases or a return to background readings.

The third key feature is that the observed resistivity increases cease at approximately 10 m depth across all three lines, matching the expected migration behavior based on the conceptual geologic model. Supporting this interpretation, the core logs and resistivity models show that the aquifer interval is capped by a thick, ubiquitous, low permeability clay diamict that extends to a depth of 10-12 m bgs, the presence of which appears to prevent further upwards migration of methane gas. This observation agrees with the findings of previous studies, particularly Lundegarde and Labreque's (1998) air sparging experiment into glacial till, where the gas remained trapped beneath an assumed low permeability layer. It is interpreted that the gas has formed a thin layer beneath this clay layer, resulting in laterally continuous increases in resistivity, most notably on day 49.

Lastly, if the changes are interpreted to be due to the presence of gas, there is evidence of significant lateral migration, between 75-100 m, in directions upgradient, downgradient, and orthogonal to the groundwater flow direction. Consequently, it would seem that vertical heterogeneity and the distribution of low permeability layers is the most influential factor to the migration pathway. There is also evidence that the lateral migration occurs earlier parallel to the groundwater flow direction, as resistivity increases are seen on Line 1 2.5 m upgradient of the injection as early as day 9. The resistivity inversions of the background data suggest that the channelized geology runs parallel to Line 1 and the groundwater flow direction. This is supported by the more laterally continuous nature of the high resistivity structure that

corresponds to our fine-grained aquifer sands. Correspondingly, Line 3 shows more lateral heterogeneity of the high resistivity structure suggesting that the profile intersects the channels orthogonally. Based on this geological interpretation, the gas first migrates updip along the direction of the channels. Resistivity increases in the orthogonal direction (Line 3) are then observed to begin spreading laterally after day 23. This suggests that the gas began 'spilling' over into adjacent channel features as the injection progressed. This has potentially significant implications when considering a natural gas leak from an energy well bore. If the subsurface environment of the well bore shows extensive heterogeneity both vertically and horizontally, the fate of the gas plume could be far afield from the aperture of an early warning monitoring installation. Thus, a detailed understanding of the subsurface geology around the wellbore is required to provide insight into potential migration pathways and assist in the efficient design of a monitoring network.

6.2 Conclusions

Electrical resistivity tomography has been successfully implemented in previous studies, as a technique for monitoring the development of immiscible fluids, such as air sparging (Lundegard and Labreque, 1995 & 1998), remediation of DNAPLs (Daily and Ramirez, 1995), and sequestration of carbon dioxide (Schmidt-Hattenberger et al., 2013). However, using ERT to monitor the migration and fate of injected methane gas is currently restricted to the study of Steelman et al (2017). In that study, they were able to successfully image the methane plume near the injection location, as well as imaging a lobe of the plume that had migrated downgradient using ERT. However, the site was a relatively homogeneous unconfined sand

aquifer, and Steelman et al. (2017) noted that migration pathways followed subtle changes in grain size where the sediment comprised of coarser grains.

Characteristic behaviour of immiscible fluids highlighted by other studies include the propensity of the fluid to migrate under buoyancy forces, in the case of DNAPLs (Daily and Ramirez, 1995) the flow was downwards. Less dense fluids, such as methane, will flow upwards as was seen by Steelman et al. (2017). Furthermore, the immiscible fluids' migration pathway is heavily influenced by impermeable layers within the subsurface (Brewster et al., 1995 and Lundegard and Labreque, 1998), and extensive lateral migration can be seen when further vertical movement is prohibited.

The study presented here expands this area of research to look at the migration of methane gas in a subsurface environment similar to that of western Canada's unconventional gas resources, specifically, a heterogeneous glacial till environment. In our study, three permanently installed ERT lines recorded time-lapse data of a controlled methane injection, with the objective of observing resistivity changes through time to further test the viability of ERT as a monitoring strategy for methane gas migration. Increases in resistivity were observed in the time-lapse difference images that are interpreted to be due to the presence of gas. The free phase gas initially migrated upwards due to buoyancy forces until reaching the low permeability clay layer that confines the aquifer. The gas plume then migrated updip in the direction of interpreted channel features for approximately 75 m. Migration into adjacent channel features in a NE direction was then observed during later surveys. The saturation of gas was observed to increase during injection, indicated by increased changes in resistivity. A possible decrease in saturation was observed after day 62 perhaps indicating dissolution of gas, gas escape to surface, migration of gas outside the experimental window, or biodegradation. After the injection gas saturation

returned to background levels. The results suggest that the migration direction was heavily influenced by variations in permeability due to the channelized depositional structure and that extensive lateral migration occurred beneath low permeability layers.

6.3 Future Work and Recommendations

Future work on this experiment should include further ERT surveys to determine the residence time of the gas in the aquifer and whether the resistivity profiles eventually return completely to background levels. The time-lapse inversions could be re-run utilizing some of the more sophisticated techniques mentioned in Haley et al. (2011) to increase the confidence in the results. This would also be an ideal data set to test the differences between different time-lapse inversion techniques.

For future experiments of this type we would like to provide several recommendations. When collecting a pre-injection data set, it is essential to complete multiple surveys. Having a pre-injection data set that is the average over several surveys compensates for natural variations and provides a standard deviation estimate of these natural variations. If possible, a remotely operated ERT acquisition unit is recommended. The use of which will increase the time-density of surveys and provide a more continuous evolution of the gas plume through time. Finally, 2D lines can be affected by out of plane resistivity anomalies, therefore, a 3D ERT array would provide greater detail and provide a more complete picture of the prominent migration directions and pathways.

The integration of multidisciplinary data to this initial geophysical work can provide greater clarity to the migration process and increase the confidence in the inversion results.

Groundwater data can give an indication to the changes in TDS, signaling gas dissolution. Microbiology data combined with the groundwater data can provide an indication as to whether biodegradation has begun by looking for methanotrophs and indication of increased acidity or TDS from the biological reactions. Surface efflux data can also provide an indication of gas escape at surface and possibly estimate associated volumes of escaped gas.

References

Adepelumi, A.A., Yi, M.J., Kim, J.H., Ako, B.D. and Son, J.S., 2006. Integration of surface geophysical methods for fracture detection in crystalline bedrocks of southwestern Nigeria. Hydrogeology Journal, 14(7), pp.1284-1306.

Archie, G.E., 1942. The electrical resistivity log as an aid in determining some reservoir characteristics. Transactions of the AIME, 146(01), pp.54-62.

Asquith, G. and Krygowski, D., 1982. Basic Well Log Analysis 2nd Edition. AAPG. Tulsa, USA.

Atekwana, E.A., Sauck, W.A. and Werkema Jr, D.D., 2000. Investigations of geoelectrical signatures at a hydrocarbon contaminated site. Journal of applied Geophysics, 44(2-3), pp.167-180.

Atekwana, E.A., Sauck, W.A., Abdel Aal, G.Z. and Werkema Jr, D.D., 2002. Geophysical investigation of vadose zone conductivity anomalies at a hydrocarbon contaminated site: implications for the assessment of intrinsic bioremediation. Journal of Environmental & Engineering Geophysics, 7(3), pp.103-110.

Atekwana, E.A., Atekwana, E.A., Rowe, R.S., Werkema Jr, D.D. and Legall, F.D., 2004. The relationship of total dissolved solids measurements to bulk electrical conductivity in an aquifer contaminated with hydrocarbon. Journal of Applied Geophysics, 56(4), pp.281-294.

Auken, E., Doetsch, J., Fiandaca, G., Christiansen, A.V., Gazoty, A., Cahill, A.G. and Jakobsen, R., 2014. Imaging subsurface migration of dissolved CO2 in a shallow aquifer using 3-D time-lapse electrical resistivity tomography. Journal of Applied Geophysics, 101, pp.31-41.

B.C. Oil and Gas Commission, 2016. British Columbia's Oil and Gas Reserves and Production Report.

Bear, J., 1972. Dynamics of fluids in porous media. Courier Corporation.

Boothroyd IM, Almond S, Qassim SM, Worrall F, Davies RJ, 2016. Fugitive emissions of methane from abandoned, decommissioned oil and gas wells. Sci Total Environ 547:461–469.

Brewster, M.L., Annan, A.P., Greenhouse, J.P., Kueper, B.H., Olhoeft, G.R., Redman, J.D. and Sander, K.A., 1995. Observed migration of a controlled DNAPL release by geophysical methods. Groundwater, 33(6), pp.977-987.

Cahill, A.G., Beckie, R., Ladd, B., Sandl, E., Goetz, M., Chao, J., Soares, J., Manning, C., Chopra, C., Finke, N. and Hawthorne, I., 2019. Advancing knowledge of gas migration and fugitive gas from energy wells in northeast British Columbia, Canada. Greenhouse Gases: Science and Technology.

Cockett, R., Kang, S., Heagy, L.J., Pidlisecky, A. and Oldenburg, D.W., 2015. SimPEG: An open source framework for simulation and gradient based parameter estimation in geophysical applications. Computers & Geosciences, 85, pp.142-154.

Cramer, B., Poelchau, H.S., Gerling, P., Lopatin, N.V. and Littke, R., 1999. Methane released from groundwater: the source of natural gas accumulations in northern West Siberia. Marine and Petroleum Geology, 16(3), pp.225-244.

Dahlin, T. and Zhou, B., 2006. Multiple-gradient array measurements for multichannel 2D resistivity imaging. Near Surface Geophysics, 4(2), pp.113-123.

Dailey, W. and Ramirez, A., 1996. Electrical impedance tomography of the 1995 OGI perchloroethelyne release (No. UCRL-ID-125461). Lawrence Livermore National Lab., CA (United States).

Davies, R.J., Almond, S., Ward, R.S., Jackson, R.B., Adams, C., Worrall, F., Herringshaw, L.G., Gluyas, J.G. and Whitehead, M.A., 2014. Oil and gas wells and their integrity: Implications for shale and unconventional resource exploitation. Marine and Petroleum Geology, 56, pp.239-254.

Ellis, R.G. and Oldenburg, D.W., 1994. Applied geophysical inversion. Geophysical Journal International, 116(1), pp.5-11.

Eltschlager, K. K., Hawkins, J. W., Ehler, C. & Baldassare, F., 2001. Technical Measures for the Investigation and Mitigation of Fugitive Methane Hazards in Areas of Coal Mining. Office of Surface Mining Reclamation and Enforcement.

Hartman, G.M. and Clague, J.J., 2008. Quaternary stratigraphy and glacial history of the Peace River valley, northeast British Columbia. Canadian Journal of Earth Sciences, 45(5), pp.549-564.

Hayley, K., Bentley, L.R., Gharibi, M. and Nightingale, M., 2007. Low temperature dependence of electrical resistivity: Implications for near surface geophysical monitoring. Geophysical research letters, 34(18).

Hayley, K., Bentley, L.R. and Pidlisecky, A., 2010. Compensating for temperature variations in time-lapse electrical resistivity difference imaging. Geophysics, 75(4), pp.WA51-WA59.

Hayley, K., Pidlisecky, A. and Bentley, L.R., 2011. Simultaneous time-lapse electrical resistivity inversion. Journal of Applied Geophysics, 75(2), pp.401-411.

Hwang, D., Yoon, D.J., Kwon, I.B., Seo, D.C. and Chung, Y., 2010. Novel auto-correction method in a fiber-optic distributed-temperature sensor using reflected anti-Stokes Raman scattering. Optics express, 18(10), pp.9747-9754.

Ingraffea, A.R., Wells, M.T., Santoro, R.L. and Shonkoff, S.B., 2014. Assessment and risk analysis of casing and cement impairment in oil and gas wells in Pennsylvania, 2000–2012. Proceedings of the National Academy of Sciences, p.201323422.

Kemna, A., Vanderborght, J., Kulessa, B. and Vereecken, H., 2002. Imaging and characterisation of subsurface solute transport using electrical resistivity tomography (ERT) and equivalent transport models. Journal of Hydrology, 267(3-4), pp.125-146.

Klazinga, D.R., 2018. Numerical investigation of the geophysical response to methane migration in an unconfined aquifer with implications for hydrocarbon wellbore leakage (Master's thesis, University of Waterloo).

LaBrecque, D.J., Owen, E., Dailey, W. and Ramirez, A.L., 1992. Noise and occam's inversion of resistivity tomography data. In SEG Technical Program Expanded Abstracts 1992 (pp. 397-400). Society of Exploration Geophysicists.

LaBrecque, D.J. and Yang, X., 2001. Difference inversion of ERT data: A fast inversion method for 3-D in situ monitoring. Journal of Environmental & Engineering Geophysics, 6(2), pp.83-89.

Lal, R., 2007. Carbon sequestration. Philosophical Transactions of the Royal Society B: Biological Sciences, 363(1492), pp.815-830.

Leverett, M., 1941. Capillary behavior in porous solids. Transactions of the AIME, 142(01), pp.152-169.

Loke, M.H., 2004. Tutorial: 2-D and 3-D electrical imaging surveys.

Loke, M.H., 2008. RES2DINV version 3.54-Rapid 2D resistivity and IP inversion using the least-squares method: Geoelectrical Imaging 2-D and 3-D. Geotomo Software, Malaysia, 130p.

Lundegard, P.D. and LaBrecque, D., 1995. Air sparging in a sandy aquifer (Florence, Oregon, USA): Actual and apparent radius of influence. Journal of Contaminant Hydrology, 19(1), pp.1-27.

Lundegard, P.D. and LaBrecque, D.J., 1998. Geophysical and hydrologic monitoring of air sparging flow behavior: Comparison of two extreme sites. Remediation Journal, 8(3), pp.59-71.

Mavko, G., Mukerji, T. and Dvorkin, J., 2009. “Electrical properties,” in The Rock Physics Handbook: Tools for Seismic Analysis of Porous Media. 2nd edn. Cambridge: Cambridge University Press, pp. 414–436. doi: 10.1017/CBO9780511626753.010.

Miller, C.R., Routh, P.S., Brosten, T.R. and McNamara, J.P., 2008. Application of time-lapse ERT imaging to watershed characterization. Geophysics, 73(3), pp.G7-G17.

Newmark, R.L., Daily, W.D., Kyle, K.R. and Ramirez, A.L., 1998. Monitoring DNAPL pumping using integrated geophysical techniques. Journal of Environmental and Engineering Geophysics, 3(1), pp.7-13.

Nguyen, F., Kemna, A., Antonsson, A., Engesgaard, P., Kuras, O., Ogilvy, R., Gisbert, J., Jorreto, S. and Pulido-Bosch, A., 2009. Characterization of seawater intrusion using 2D electrical imaging. Near Surface Geophysics, 7(5-6), pp.377-390.

Pidlisecky, A., Haber, E. and Knight, R., 2007. RESINVM3D: A 3D resistivity inversion package. Geophysics, 72(2), pp.H1-H10.

Pidlisecky, A. and Knight, R., 2008. FW2_5D: A MATLAB 2.5-D electrical resistivity modeling code. Computers & Geosciences, 34(12), pp.1645-1654.

Rivard, C., Lavoie, D., Lefebvre, R., Séjourné, S., Lamontagne, C. and Duchesne, M., 2014. An overview of Canadian shale gas production and environmental concerns. International Journal of Coal Geology, 126, pp.64-76.

Rogers, A.J., 1991, September. Distributed optical fiber sensing. In Chemical and Medical Sensors (Vol. 1510, pp. 2-25). International Society for Optics and Photonics.

Rosqvist, H., Johansson, S., Dahlin, T., Leroux, V. and Svensson, M., 2011-a. Development of 3D geoelectrical resistivity for mapping of gas migration in landfills. In Proceedings Sardinia-11, Thirteen International Waste Management and Landfill Symposium, Italy.

Rosqvist, H., Leroux, V., Dahlin, T., Svensson, M., Lindsjö, M., Månsson, C.H. and Johansson, S., 2011-b. Mapping landfill gas migration using resistivity monitoring. Waste and Resource Management, 164(1), pp.3-15.

Sauck, W.A., 2000. A model for the resistivity structure of LNAPL plumes and their environs in sandy sediments. Journal of Applied Geophysics, 44(2-3), pp.151-165.

Schmidt-Hattenberger, C., Bergmann, P., Bösing, D., Labitzke, T., Möller, M., Schröder, S., Wagner, F. and Schütt, H., 2013. Electrical resistivity tomography (ERT) for monitoring of CO2 migration-from tool development to reservoir surveillance at the Ketzin pilot site. Energy Procedia, 37, pp.4268-4275.

Slater, L., Comas, X., Ntarlagiannis, D. and Moulik, M.R., 2007. Resistivity-based monitoring of biogenic gases in peat soils. Water resources research, 43(10).

Steelman, C.M., Klazinga, D.R., Cahill, A.G., Endres, A.L. and Parker, B.L., 2017. Monitoring the evolution and migration of a methane gas plume in an unconfined sandy aquifer using time-lapse GPR and ERT. Journal of contaminant hydrology, 205, pp.12-24.

Telford, W.M., Telford, W.M., Geldart, L.P., Sheriff, R.E. and Sheriff, R.E., 1990. Applied geophysics (Vol. 1). Cambridge university press.

Terry, N., Slater, L., Comas, X., Reeve, A.S., Schäfer, K.V. and Yu, Z., 2016. Free phase gas processes in a northern peatland inferred from autonomous field-scale resistivity imaging. Water Resources Research, 52(4), pp.2996-3018.

Thomson, N.R. and Johnson, R.L., 2000. Air distribution during in situ air sparging: an overview of mathematical modeling. Journal of hazardous materials, 72(2-3), pp.265-282.

Van Stempvoort, D., Maathuis, H., Jaworski, E., Mayer, B. and Rich, K., 2005. Oxidation of fugitive methane in ground water linked to bacterial sulfate reduction. Groundwater, 43(2), pp.187-199.